Modeling of embankment beneath marine deposited soft sensitive clays considering straightforward creep degradation

Qi-Yin ZHU[1], Yin-Fu JIN[1,2,*], and Zhen-Yu YIN[1,2]

Affiliations:

[1] State Key Laboratory for Geomechanics & Deep Underground Engineering, China University of Mining & Technology, Xuzhou 221116, China

[2] Department of Civil and Environmental Engineering, The Hong Kong Polytechnic University, Hung Hom, Kowloon, Hong Kong

[*] Corresponding author: Dr. Yin-Fu Jin, Tel: +852 3400 8470, email: yinfu.jin9019@gmail.com

Abstract: One method describing the creep degradation behavior of marine deposited soft structured clay straightforwardly is proposed and applicated to the embankment modeling. Based on the experimental phenomena, the evolution of creep coefficient of soft structured clay is identified comparing with reconstituted clay, and formulated by the creep coefficient of reconstituted clay and a creep based structured parameter. This parameter evolves with the development of viscoplastic strain which related to the inter-particle bonding. Thus, the contributions of the inter-particle bonding and debonding for soft structured clays to creep coefficient is considered and the creep degradation behavior is captured straightforwardly. The creep coefficient is extended to 3D and incorporated into a newly developed model to describe the creep degradation in a straightforward way. Based on the correlations, the liquid limit is adopted as the viscosity input parameter. Newton-Raphson algorithm of the model is derived and implemented into a Finite Element code for coupled consolidation analysis. The predictive ability on creep degradation of the model is validated by simulating 1D creep test. 1D CRS (constant strain rate) and 3D undrained creep tests are also modelled to show the calculation ability of the code. Finally, the new model considering creep degradation is applicated to simulate the Murro test embankment, and Gloucester test fill which are constructed on marine deposited soft sensitive clays.

Keywords: clays; viscoplasticity; creep; destructuration; liquid limit; embankment.

1 Introduction

Marine sedimentation can bring about large pores and flocculation structure, resulting in a strong structural structure of the soil (Mitchell and Soga 2005). Such marine deposited soil exhibits high compressibility, low strength, high sensitivity, and significant creep behaviours (Yin et al 2011), which can reduce the safety and service life of constructions. Similar deposits can also be found in other parts of Europe, North America, and Asia (Yin, Hattab, Hicher 2011). The construction on soft structured marine soil deposits has become increasingly important in past decades, as more and more development occurs on areas that were considered unsuitable for construction just a few decades ago (Karstunen and Yin 2010, Chai et al 2013, Zhang et al 2015). The current design methods are very crude, in most cases over conservative, but in some cases unsafe. Therefore, safe and economical design and construction on marine deposited soft structured soils has become an important issue.

Finite element modeling is usally conducted to assist in the design of the embankments, and the constitutive model plays an important role in the modeling (Jamsawang et al. 2018; Müthing et al. 2018; Rezania et al. 2017). The Modified Cam Clay model (Roscoe and Burland 1968) capturing the main features of soft soils with fewer parameters was usually adopted in some studies (Indraratna et al. 1997; Huang et al. 2006; Bergado and Teerawattanasuk 2008; Chai et al. 2013; Nunez, Briançon, and Dias 2013; Dai, Chen, and Qin 2017). Within the elastic plastic framework, more sophisticated models based on the MCC model were developed and used in modeling of embankment (Karstunen et al. 2005, 2006; Tanchaisawat, Bergado, and Voottipruex 2008; Borges and Marques 2011; D'Ignazio, Lansivaara, and Jostad 2017; Araújo, Palmeira, and Macêdo 2012; Panayides, Rouainia, and Wood 2012). However, natural marine soft soils exhibit significant creep behavior under both laboratory and field conditions after primary consolidation. Thus, recently more finite element analysis of embankment employed elastic-viscoplastic models based on the creep phenomenon (Karim et al. 2010; Kelln et al. 2009; Zhu and Yin 2012; Karlsson,

Emdal, and Dijkstra 2016) or rate-dependency of soils (Kim and Laroueil 2001; Hinchberger and Qu 2009; Hinchberger and Rowe 1998, 2005; Rowe and Li 2002). In these simulations, few of them considered the creep degradation of marine deposited soft sensitive clays (Karstunen and Yin 2010).

The creep coefficient, defined as $C_{\alpha e}= \Delta e/\Delta \ln t$ (e and t represent void ratio and time, respectively) based on oedometer creep testing, is a key parameter for engineering practice and modeling. This coefficient is generally not constant but decreases progressively with the destructuration of soil structure as demonstrated by Mesri and Godlewski (1977), Leroueil et al. (1985), Karstunen and Yin (2010), Yin et al. (2011) and Yin, Hattab, and Hicher (2011). Numerous test results showed the soil structure destructuration results in large deformation, which can cause the creep degradation with a nonlinear consecutively decreasing $C_{\alpha e}$ fully related to the soil density (Yin, Xu and Yu 2015). This physical phenomenon is termed as creep degradation by Zhu et al. (2017) and Yin, Zhu, and Zhang (2017), and we will keep this denomination in the following text.

The creep degradation was usually modelled by strain-rate dependency based models by incorporating an intrinsic static or reference surface with a structure parameter defined in stress space (Yin et al. 2011; Rocchi, Fontana, and Da Prat 2003, Kimoto and Oka 2005). During last decades, various elastic viscoplastic models were also proposed based on the creep phenomena using $C_{\alpha e}$ explicitly as a key parameter in constitutive equations (Yin and Graham 1989; Vermeer and Neher 1999; Yin, Zhu, and Graham 2002; Leoni, Karstunen, and Vermeer 2008; Yin, Xu, and Yu 2015; Yin et al. 2016; Jin et al. 2017). These creep based models have generally more advantage in parameters determination comparing to others (Yin et al. 2010). Zhu et al. (2016) recently presented a straight way to describe the evolution of $C_{\alpha e}$ with the soil structure under one-dimensional condition which can be incorporated into the model presenting in Yin, Xu, and Yu (2015). Thus, the creep degradation can be modelled in a more direct way and these creep models

can be extended.

This paper attempts to propose an enhanced elastic viscoplastic model and study the embankment considering creep degradation. For this, we first investigate phenomena of creep degradation based on experiments, and $C_{\alpha e}$ of intact marine deposited clays is formulated by a structure parameter. The new $C_{\alpha e}$ is incorporated into an anisotropic elastic viscoplastic model to describe the creep degradation. Some new parameters are correlated with liquid limit for the convenience. Then, the Newton-Raphson algorithm of the model is introduced and the second derivative of yield function with respect to stress is derived. After that, the model is implemented into a Finite Element code, by which the coupled consolidation analysis can be carried out. The well documented Murro test embankment is first simulated by the proposed model with a creep parameter. The Gloucester test fill is further simulated to confirm the applicability of the proposed model on embankment with creep degradation.

2. Enhancement of ANICREEP model

2.1 Phenomena of creep degradation

Conventional oedometer tests on various reconstituted soft clays show that the creep coefficient $C_{\alpha e}$ deceases linearly with the deceasing of void ratio (e) in double logarithmic plane as illustrated in Fig. 1 (Yin, Xu, and Yu 2015; Zhu et al. 2016). Since the influence of soil structure to $C_{\alpha e}$ is eliminated for reconstituted samples, the void ratio (e) can be used as a physical state of soils representing the soil density and the deformation potential (Yin 1999). The creep degradation formulation based on Fig. 1 as proposed by Yin, Xu, and Yu (2015) can be adopted:

$$\frac{C_{\alpha e}}{C_{\alpha ef}} = \left(\frac{e}{e_f} \right)^m \tag{1}$$

where $C_{\alpha ef}$ and e_f are reference values of $C_{\alpha e}$ and e, respectively (the initial in-situ void ratio e_0 was used as e_f by Yin, Xu, and Yu (2015)); m is a material constant representing the slope of the

log($C_{\alpha e}$)-log(e) curve which can be measured straightforwardly. It is worth pointing out that, $C_{\alpha e}$ is defined as the slope of the secondary consolidation line with the logarithm of time, which is suitable for design purpose in geotechnical engineering within a limited time period, but resulting in a non-positive void ratio during creep under long periods of time. Whereas, Eq. (1)imposes a value of e converging towards zero but remaining always positive.

The reference point ($C_{\alpha ef}$, e_f) can be arbitrary selected. However, it could be interesting to select specific value as the reference void ratio. The void ratio at the liquid limit (e_L) is usually adopted to establish the equations for compressibility and can be easily determined by liquid limits (w_L) and specific gravity (G_s) , both of which are available physical properties of clayey soils (Nagaraj and Murthy 1983). Along the line in Fig. 1, the point (e_L, $C_{\alpha eL}$) can be used as a reference. Thus, Eq. (1) can be rewritten as

$$C_{\alpha e} = C_{\alpha eL}\left(\frac{e}{w_L G_s}\right)^m \tag{2}$$

During conventional oedometer tests on intact samples of intact soft clays, the shape of the post-yield compression curve is significantly influenced by the debonding process during straining. Fig. 2a shows the schematic plot of the compression curves of intact and reconstituted clay samples. For a given inelastic strain level $\Delta\varepsilon^{vp}$, the bond degradation results in the current stress σ'_v reaching point A. Corresponding to the stress σ'_v at $\Delta\varepsilon^{vp}$, there exsits an intrinsic stress σ'_{vi}, which is the stress for a reconstituted sample at the same inelastic strain increment (point B). When the strain increases, the inter-particle bonds are progressively broken and the compression curve for intact clay gradually approach to the compression curve for reconstitutive clay, as shown in Fig. 2a.

Experiment results show that the creep coefficient $C_{\alpha e}$ from intact samples is generally larger than that of reconstituted sample. The difference between the values of $C_{\alpha e}$ for intact and reconstituted sample is assumed for the effect of soil structure and its destructuration. At the stress

level with viscoplastic strain $\Delta\varepsilon^{vp}$, creep coefficients $C_{\alpha e}$(I) and $C_{\alpha e}$(R) corresponding to σ'_v and σ'_{vi}, respectively, can be determined. According to their definitions, $C_{\alpha e}$(I) is directly determined from experimental results while $C_{\alpha e}$(R) is estimated by Eq.(1) under the same viscoplastic strain level. Similarly, creep coefficients for intact and reconstituted samples at different viscoplastic strain levels can be plotted by $C_{\alpha e}$ versus void ratio, as schematically shown in Fig. 2b. It can be seen that the $C_{\alpha e}$(I) is more strain dependent than $C_{\alpha e}$(R). In this paper, the contribution of the soil structure and destructuration to the creep coefficient can be expressed by a new structure parameter ρ based on creep instead of stress

$$\rho = \frac{C_{\alpha e}(I)}{C_{\alpha e}(R)} - 1 \tag{3}$$

where ρ is always positive with an initial value of $\rho_0 = C_{\alpha e0}(\mathrm{I})/C_{\alpha e0}(\mathrm{R}) - 1$ and decreases from its initial value ρ_0 towards zero with the inter-particle debonding till to all the bonds destroyed completely.

Furthermore, according to the definition of ρ the normalized degradation ρ/ρ_0 with the viscoplastic strain (ε^{vp}) can be plotted in Fig. 2c for different clays (Zhu et al. 2016). An exponential formulation can be adopted:

$$\rho = \rho_0 \exp\left(-\xi \cdot \varepsilon^{vp}\right) \tag{4}$$

where ξ is a material constant controlling the degradation rate of ρ.

Combing Eqs (2), (3) and (4), the creep coefficient for intact marine soft clays can be written:

$$C_{\alpha e} = \left(\rho_0 \exp\left(-\xi \cdot \varepsilon^{vp}\right) + 1\right) C_{\alpha eL} \left(\frac{e}{w_L G_s}\right)^m \tag{5}$$

Eq.(5) indicates that $C_{\alpha e}$ depends on the material constants $C_{\alpha eL}$, m, ρ_0 and ξ; the viscoplastic strain level ε^{vp}, the state variable e and the physical properties w_L and G_s.

2.2 Elastic viscoplastic model considering creep degradation

The model proposed in this paper is based on the ANICREEP model (Yin et al. 2010). A brief description of the model ANICREEP can be found in Appendix. This model is developed based on the overstress viscoplastic theory by Perzyna (1966). The viscoplastic strain rate was formulated as follows,

$$\dot{\varepsilon}_{ij}^{vp} = \frac{C_{\alpha e}}{(1+e_0)\tau}\frac{\left(M_c^2-\alpha_{K0}^2\right)}{\left(M_c^2-\eta_{K0}^2\right)}\left(\frac{p_m^d}{p_m^r}\right)^{\frac{\lambda-\kappa}{C_{\alpha e}}}\frac{\partial f_d}{\partial \sigma_{ij}'} \tag{6}$$

where notations can be found in Appendix. Eq.(6) is derived through a rigorous formula and the parameters have a clear physical meaning Yin et al. 2010). The model principle in p'-q plane is illustrated in Fig. 3.

In order to model the creep degradation of marine deposited soft clay, two modifications need to be carried out:

a) the creep coefficient $C_{\alpha e}$ in Eq.(6) needs to be replaced by a simple three-dimensional extension of Eq.(5) (the use of viscoplastic strain same as Kimoto and Oka (2005)) as follows,

$$C_{\alpha e} = \left(\rho_0 \exp\left[-\xi\sqrt{\varepsilon_{ij}^{vp}:\varepsilon_{ij}^{vp}}\right]+1\right)C_{\alpha eL}\left(\frac{e}{w_L G_s}\right)^m \tag{7}$$

b) according to (Yin and Wang 2012), the strain-rate parameter ($\beta = (\lambda\text{-}\kappa)/C_{\alpha e}$ in Eq.(6)) should be constant for soft sensitive clays. Thus, the λ in Eq.(6) needs to be replaced by the following equation with λ_L representing the compressibility coefficient of reconstituted clay (the same as λ of insensitive clay)

$$\lambda = \left(\rho_0 \exp\left[-\xi\sqrt{\varepsilon_{ij}^{vp}:\varepsilon_{ij}^{vp}}\right]+1\right)\left(\lambda_L-\kappa\right)+\kappa \tag{8}$$

Then, different from ANICREEP model, the creep input parameter $C_{\alpha e}$ is replaced by $C_{\alpha eL}$,

w_L and m, and two additional parameters ρ_0 and ξ are further required.

2.3 Parameters determination for creep degradation

The creep behavior is tightly connected to the intrinsic properties of clay, such as the shape and size of particle, the inter/intra-aggregate pore size distribution and the double layer, which can be characterized by Atterberg limits (Mitchell and Soga, 2005). Thus, the correlations between material constants relating to creep degradation (Eq. (7)) and Atterberg limits are investigated based on available results in literature, considering that such correlations would be useful for engineering practice. Due to the broad practicability of w_L, the following correlations of model parameters with Atterberg limits is based on w_L. Considering the emphasis of this paper, the correlation process is simplified and more details can be found in (Zhu et al. 2016).

The material constants $C_{\alpha eL}$ and m can be determined from tests on reconstituted clay. Fig. 4a plots the correlation between $C_{\alpha eL}$ and w_L, from which the following relation could be obtained with a correlation coefficient $R^2 = 0.9336$

$$C_{\alpha eL} = 0.0007 w_L - 0.0223 \tag{9}$$

Fig. 4b presents the plot of the fitting of m with w_L, with the equation expressed as

$$m = 0.0157 w_L - 0.2418 \tag{10}$$

where the correlation coefficient is $R^2 = 0.3964$. We can see that all data points are in the range of plus or minus 0.4 of the correlated value. Considering the correlation coefficient of m is lower, a simple sensitively analysis of m was conducted on a typical intact clay (Vanttila clay with w_L = 90 %). Fig. 4c plots the comparisons of $C_{\alpha e}$ with the experimental results and the estimated values with m = 1.17 obtained by Eq.(10) and m = 1.17±0.4. Considering that the change of $C_{\alpha e}$ within a reasonable value of m is rather small, the deviation of creep induced by m is slight and can be neglected.

As mentioned above, ρ_0 is the initial value of ρ and it represents the creep degradation potential induced by debonding. Due that soil sensitivity S_t is commonly adopted in geotechnical engineering, a certain relationship between ρ_0 and S_t was observed (Fig.4c, from Zhu et al. 2016) and the expression with a correlation coefficient $R^2 = 0.7641$ is adopted:

$$\rho_0 = 2.34\left(S_t - 1\right)\exp\left(-0.047 w_L\right) \tag{11}$$

Then, only S_t, w_L and ξ are further required as input parameters relating to the creep and its degradation.

Furthermore, the parameters for creep degradation can also be determined by optimization-based parameter identification (Ye et al. 2016, Jin et al., 2017, Yin et al. 2017, 2018) from conventional triaxial tests.

3. Implementation and validation

The model was integrated using the Newton-Raphson algorithm and implemented as a user-defined model in the 2D Version of PLAXIS for a coupled consolidation analysis based on Biot's theory.

3.1 Newton-Raphson algorithm

With the formulations in Appendix, a general elasto-viscoplastic constitutive relation can be obtained by

$$\dot{\boldsymbol{\sigma}} = \boldsymbol{D}\left(\dot{\boldsymbol{\varepsilon}} - \dot{\boldsymbol{\varepsilon}}^{vp}\right) \tag{12}$$

where $\boldsymbol{D}$ is elastic moduli. Based on Eq. A[5], the increment rate of hardening parameter could be expressed by

$$\dot{p}_m^r = p_m^r \frac{1+e_0}{\lambda - \kappa}\dot{\varepsilon}_v^{vp} \tag{13}$$

Integrating Eqs. (12) and (13) over time step Δt, i.e., from time t_n to $t_{n=1}$, gives

$$\Delta\boldsymbol{\sigma} = \boldsymbol{D}\Delta\boldsymbol{\varepsilon} - \boldsymbol{D}\Delta\boldsymbol{\varepsilon}^{vp} \tag{14}$$

and

$$\Delta p_m^r = \mu\left(\frac{p_m^d}{p_m^r}\right)^{\beta} h \quad \text{with} \quad h = p_m^r \frac{1+e_0}{\lambda-\kappa}\frac{\partial f_d}{\partial p'} \tag{15}$$

where $\Delta\boldsymbol{\sigma} = \boldsymbol{\sigma}^{n+1} - \boldsymbol{\sigma}^n$ with $\boldsymbol{\sigma}^n = \boldsymbol{\sigma}(t_n)$; similar definitions hold true for $\Delta\boldsymbol{\varepsilon}$ and Δp_m^r . Combining Eqs. (14) and (15), a group of equations can be obtained as

$$\boldsymbol{G} = \begin{cases} \boldsymbol{\sigma}^{n+1} - \boldsymbol{\sigma}^{tr} + \boldsymbol{D}\Delta\boldsymbol{\varepsilon}^{vp} \\ p_m^{r,n+1} - p_m^{r,n} - \mu\Phi h \end{cases} \tag{16}$$

where $\boldsymbol{\sigma}^{tr} = \boldsymbol{D}\Delta\boldsymbol{\varepsilon}$ is the trial elastic stress tensor, which is assumed to be constant in a time step. The solutions of $\boldsymbol{\sigma}^{n+1}$ and $p_m^{r,n+1}$ could be solved by an iterative procedure with Newton-Rapshon method. The corrected values of $\delta\boldsymbol{\sigma}$ and δp_m^r is obtained by an iteration loop and calculated by $\delta\boldsymbol{x} = -\left(\boldsymbol{J}\right)^{-1}\boldsymbol{G}$, in which $\boldsymbol{J} = \partial\boldsymbol{G}/\partial\boldsymbol{x}$ is Jacobian matrix with $\boldsymbol{x} = \left\{\boldsymbol{\sigma}, p_m^r\right\}^T$. The iteration loop comprises: (a) calculate $\boldsymbol{G}^i$ and $\boldsymbol{J}^i$ according to $\boldsymbol{x}^i$; (b) calculate $\delta\boldsymbol{x}^i = -\left(\boldsymbol{J}^i\right)^{-1}\boldsymbol{G}^i$, then update $\boldsymbol{x}^{i+1} = \boldsymbol{x}^i + \delta\boldsymbol{x}^{i+1}$. Steps (a) and (b) will be repeated until $\Sigma G_i^i < Tol$ and $\Sigma\delta x_i^i < Tol$. The superscript i represents the number of iteration, the subscript i represents the number of component and Tol is the tolerance value. After the convergence is achieved, the stresses and hardening parameters are updated. The flow chart for the time integration algorithm of Newton Raphson is shown in Fig. 5.

The important derivation for the algorithm is the $\partial\dot{\varepsilon}^{vp}/\partial\sigma$, expressed as

$$\frac{\partial\dot{\varepsilon}_{vp}^i}{\partial\sigma} = \frac{\mu\beta}{p_m^r}\left\langle\left(\frac{p_m^d}{p_m^r}\right)^{\beta-1}\right\rangle\frac{\partial g}{\partial\sigma}\frac{\partial f_d}{\partial\sigma} + \mu\left\langle\left(\frac{p_m^d}{p_m^r}\right)^{\beta}\right\rangle\frac{\partial^2 g}{\partial\sigma^2} \tag{17}$$

where g is the plastic potential function. Adopting the associate flow rule, that is

$$f_d = g = \frac{3}{2}\frac{\left(\sigma_d - p'\alpha_d\right):\left(\sigma_d - p'\alpha_d\right)}{\left(M^2 - {\alpha_d}^2\right)p'} + p' - p_m^d = 0 \tag{18}$$

Consequently, the key to sloving Eq. (17) is to obtain the second deviative of f_d respect to stress, that is $\partial^2 f_d / \partial\sigma^2$. Firstly, we needed to derive the partial derivatives of f_d with respect to stress, that is

$$\frac{\partial f_d}{\partial \sigma_i} = \frac{\partial f_d}{\partial \sigma_{dk}}\frac{\partial \sigma_{dk}}{\partial \sigma_i} + \frac{\partial f_d}{\partial p'}\frac{\partial p'}{\partial \sigma_i} \tag{19}$$

where the partial derivatives of f_d with respect to deviatoric and mean effective stress can be expressed by

$$\frac{\partial f_d}{\partial \sigma_{dk}} = 3\frac{\sigma_{dk} - p'\alpha_{dk}}{(M^2 - \alpha_s^2)p'} \tag{20}$$

$$\frac{\partial f_d}{\partial p'} = -3{\alpha_{dk}}^T\frac{\sigma_{dk} - p'\alpha_{dk}}{(M^2 - \alpha_s^2)p'} - \frac{3}{2}\frac{\left[\sigma_{dk} - p'\alpha_{dk}\right]^T\left[\sigma_{dk} - p'\alpha_{dk}\right]}{(M^2 - \alpha_s^2)p'} + 1 \tag{21}$$

where the superscript T denotes the transpose of a matrix. Then, the derivative of dynamic yield surface f_d with respect to stress can be derived as

$$\begin{aligned}\frac{\partial f_d}{\partial \sigma_i} = {} & 3\frac{\sigma_{dk} - p'\alpha_{dk}}{(M^2 - \alpha_s^2)p'}\frac{\partial \sigma_{dk}}{\partial \sigma_i} - 3\frac{\partial p'}{\partial \sigma_i}\alpha_{dk}^T\frac{\sigma_{dk} - p'\alpha_{dk}}{(M^2 - \alpha_s^2)p'} \\ & - \frac{3}{2}\frac{\partial p'}{\partial \sigma_i}\frac{[\sigma_{dk} - p'\alpha_{dk}]^T[\sigma_{dk} - p'\alpha_{dk}]}{(M^2 - \alpha_s^2)p'^2} + \frac{\partial p'}{\partial \sigma_i}\end{aligned} \tag{22}$$

Now, we repeat the deriving process above. Based on Eq.(22), the partial derivatives of $\partial f / \partial \sigma_i$ with respect to deviatoric and mean effective stress are given

$$\begin{aligned}\frac{\partial^2 f_d}{\partial\sigma_i\partial\sigma_{dj}^T} &= \frac{3}{(M^2-\alpha_s^2)p'}\frac{\partial\sigma_{dj}^T}{\partial\sigma_i} - \frac{3}{(M^2-\alpha_s^2)p'}\frac{\partial p'}{\partial\sigma_i}\alpha_{dj}^T \\ &\quad - \frac{3}{(M^2-\alpha_s^2)p'^2}\frac{\partial p'}{\partial\sigma_i}[\sigma_{dj}-p'\alpha_{dj}]^T \\ &= \frac{3}{(M^2-\alpha_s^2)p'}\frac{\partial\sigma_{dj}^T}{\partial\sigma_i} - \frac{3\sigma_{dj}^T}{(M^2-\alpha_s^2)p'^2}\frac{\partial p'}{\partial\sigma_i}\end{aligned} \tag{23}$$

$$\begin{aligned}\frac{\partial^2 f_d}{\partial\sigma_i\partial p'} &= -3\frac{\partial\sigma_{dk}^T}{\partial\sigma_i}\frac{\alpha_{dk}}{(M^2-\alpha_s^2)p'} - 3\frac{\partial\sigma_{dk}^T}{\partial\sigma_i}\frac{\sigma_{dk}-p'\alpha_{dk}}{(M^2-\alpha_s^2)p'^2} \\ &\quad + 3\frac{\partial p'}{\partial\sigma_i}\frac{\alpha_{dk}^T\alpha_{dk}}{(M^2-\alpha_s^2)p'} + 6\frac{\partial p'}{\partial\sigma_i}\frac{\alpha_{dk}^T[\sigma_{dk}-p'\alpha_{dk}]}{(M^2-\alpha_s^2)p'^2} \\ &\quad + 3\frac{\partial p}{\partial\sigma_i}\frac{[\sigma_{dk}-p'\alpha_{dk}]^T[\sigma_{dk}-p'\alpha_{dk}]}{(M^2-\alpha_s^2)p'^3} \\ &= -3\frac{\partial\sigma_{dk}^T}{\partial\sigma_i}\frac{\alpha_{dk}}{(M^2-\alpha_s^2)p'^2} + 3\frac{\partial p'}{\partial\sigma_i}\frac{\sigma_{dk}^T\sigma_{dk}}{(M^2-\alpha_s^2)p'^3}\end{aligned} \tag{24}$$

Then, the second order derivative of f_d with respect to stress is finally obtained

$$\begin{aligned}\frac{\partial^2 f_d}{\partial\sigma_i\partial\sigma_j^T} &= \frac{\partial^2 f}{\partial\sigma_i\partial\sigma_{dk}^T}\frac{\partial\sigma_{dk}}{\partial\sigma_j^T} + \frac{\partial^2 f}{\partial\sigma_i\partial p'}\frac{\partial p'}{\partial\sigma_j^T} \\ &= \frac{3}{(M^2-\alpha_s^2)p'}\frac{\partial\sigma_{dk}^T}{\partial\sigma_i}\frac{\partial\sigma_{dk}}{\partial\sigma_j^T} - \frac{3\sigma_{dk}^T}{(M^2-\alpha_s^2)p'^2}\frac{\partial p'}{\partial\sigma_i}\frac{\partial\sigma_{dk}}{\partial\sigma_j^T} \\ &\quad - 3\frac{\sigma_{dj}}{(M^2-\alpha_s^2)p'^2}\frac{\partial p'}{\partial\sigma_j^T} + 3\frac{\partial p'}{\partial\sigma_i}\frac{\sigma_{dk}^T\sigma_{dk}}{(M^2-\alpha_s^2)p'^3}\frac{\partial p'}{\partial\sigma_j^T}\end{aligned} \tag{25}$$

3.2 Coupled consolidation

The basic finite element scheme for the proposed model is similar to those presented by Oka, Adachi, and Okano (1986) and Hinchberger and Rowe (1998). For a coupled consolidation analysis based on Biot's theory, the relationship of the load increment is given by applying the principle of virtual work to the equilibrium equation as shown by Oka, Adachi, and Okano (1986)

$$\int_V [\Delta\varepsilon]^T \cdot [\Delta\sigma] \cdot dV = \int_V [\Delta\varepsilon]^T \cdot [\Delta\sigma'] \cdot dV + \int_V [\Delta\varepsilon]^T \cdot [\Delta u_w] \cdot dV$$
$$= \int_V [\Delta d]^T \cdot [\Delta F_b] \cdot dV + \int_S [\Delta d]^T \cdot [\Delta T] \cdot dS \tag{26}$$

The equation of continuity for water flow can be expressed as follows

$$\int_{vol} [b] \left[\sum_{i=1}^{3} \frac{k_i}{\gamma_w} \frac{\partial^2 u_w}{\partial x_i^2} + \frac{\partial v}{\partial t} \right] d(vol) = 0 \tag{27}$$

where k_i is the hydraulic conductivity in three coordinate directions, γ_w is the unit weight of the pore water, v is the seepage velocity.

When a constitutive model is implemented in a conventional stress–strain form as a user-defined soil model into Plaxis, large strain analysis with updating pore pressures can be selected for the calculation by using this module combined with the user-defined model. In this study, the analysis of embankment was performed adopting this technic. Details can also be found in Karstunen and Yin (2010).

3.3 Predictive ability on creep degradation

In order to evaluate the model's predictive ability, simulations for both 1D oedometer tests and 3D undrained creep tests on Murro clay were studied by the new enhanced model considering creep degradation.

1D creep: intact and reconstituted Murro clay

Conventional oedometer tests on reconstituted and intact sample of Murro clay from a depth of 4 m were simulated. For reconstituted clay, the destructuration parameters are not needed (S_t=1, ξ =0). For intact clay, values of parameters determined from conventional oedometer tests (Fig. 6a) and triaxial tests, used for all test simulations are summarized in Table 1. POP in the table denotes the pre-overburden stress, which is the difference between vertical preconsolidation stress

and in-situ vertical effective stress. Figs 6b and 6c shows good agreement between experiments and simulations for the settlement-time curves of conventional oedometer tests for intact and reconstituted clays. To further study the creep degradation behavior, the experimental and simulation results on the evolution of creep coefficient with vertical effective stress for both intact and reconstituted clay samples have been plotted in Fig. 6d. The comparison shows the model captured well the creep degradation trend of the experiments.

1D CRS tests were simulated and illustrated using parameters the same as Murro clay with different strain rate, soil sensitivity (S_t), and destructuration rate parameter (ξ). Fig. 7a shows three compression curves corresponding to different strain rate (strain rate = 0.04%/h, 0.4%/h and 4%/h). Because the values of destructuration parameters (S_t and ξ) are the same, these curves are apparently parallel. Fig. 7b plots three compression curves corresponding to S_t = 1, 7, 14 respectively. The curve S_t = 14 is on the bottom, representing the strain is larger than other two tests at the same stress level. This is because the predicted $C_{\alpha e}$ is larger for a higher sensitivity (based on Eqs (7) and (11)). Fig. 7c presents three compression curves corresponding to different destructuration rate parameters which represent the effect of the destructuration rate on the compression behavior of natural soft clay. When the destructuration rate parameter ξ increasing from 9 to 15, the compression curve moves above. This is reasonable because a bigger ξ reduces the value of ρ more rapider based on Eq.(4). Then, $C_{\alpha e}$ will decrease along with the decreasing of ρ and the strain is smaller for the cases with bigger ξ at the same stress level.

Overall, the proposed model can well capture the creep degradation behavior of natural soft clays during 1D tests.

3D creep: simulated trend on undrained creep

Note that no data available for triaxial undrained creep tests on Murro clay, the model was employed to simulate triaxial undrained creep tests using parameters in Table 1 to examine the

predicted trend of creep degradation in 3D condition. For the simulation, the sample was first K_0-consolidated to a vertical stress of $\sigma'_{v0} = \sigma'_{p0} = 28$ kPa for 24 hours. Then, an additional vertical stress of 17 kPa was applied for undrained creep test. The creep process lasts for 240 hours. Fig. 8 shows the simulated results for the undrained triaxial creep tests with three different initial sensitivities ($S_t = 1, 7, 14$). Generally, for higher S_t the deviatoric strain is higher (Fig. 8a). In Fig. 8b, the mean effective stress p' decreases rapidly at the early stage of the creep for the case of higher S_t, and then approaches to curves with lower S_t along with the time. The simulated results demonstrate that the creep degradation during undrained creep is highly dependent on the initial structure or sensitivity of soils, which is the case in experiments.

4. Application to embankment on soft structured clays

4.1 Murro test embankment

Finite element model

Murro test embankment is a well instrumented test embankment on a soft clay deposit in Finland, which has been studied by (Karstunen and Yin 2010; Yin, Xu, and Yu 2015; Karstunen et al. 2005). Table 2 lists the average values for physical properties of Murro clay. In the finite element analysis, the plain strain condition was assumed and the finite element mesh is shown in Fig. 9. The groundwater table is located at the depth of 0.8 m. The horizontal boundary is 36 m away from the embankment center-line and the vertical boundary is at a depth of 23 m as used in Karstunen et al. (2005). The horizontal displacements are fixed in the lateral boundaries, and the vertical and horizontal displacements are fixed at the bottom. The finite element model consists of 1456 elements resulting in 3019 nodes. The embankment fill material is crushed cork with a grain size of 0-65 mm which was modelled by Mohr-Coulomb model and typical values of model parameters are summarized in Table 3. The construction of the embankment took 2 days and the same was simulated in the modelling with the enhanced creep model and the coupled

consolidation theory presented in section 3.2.

Parameters of foundation clays

For the proposed model w_L is an important input parameter to calculate the creep degradation behavior. The average value of w_L is adopted for each layer according to the geological survey. The parameter $\xi = 7$ calibrated from Murro clay in the previous section was adopted for all soil layers. Other parameters determined in average values and used in the modelling by Karstunen and Yin (2010) were adopted (Table 4) and the details of the process of determination will not be repeated here. In order to investigate the effect of creep degradation, two additional predictions were made with different value of S_t: $S_t = 1$ and S_t equal to two times of the real S_t (marked as $2S_t$ in the following description). All results were compared each other.

Settlements

During and after construction, the extra pressure due to the fill of embankment plus the initial earth pressure determined with the weight parameters and horizontal earth coefficient K_0 would excess the yield stress of the soil. Then, large settlements will occur. Figs 10a and 10b present the simulated and observed surface settlements under the centerline (S2, S5 and S7) and 5 m away from the centerline (S4 and S6) of the embankment respectively. Comparisons show that the model with calibrated parameters (that of S_t) well captured the long-term settlement behavior of embankment. For different assumed S_t, all three cases well predicted the surface settlements in the short time. The major difference was found between the predictions after 100 days of construction. The difference became more and more significant with time. In general, the prediction with $2S_t$ results in a larger settlement since the creep rate is larger than the other two cases. All comparisons show that the consideration of creep degradation does not influence the short-term settlement behavior, but influence significantly the long-term settlement behavior. Comparions with the predicted results by Yin, Xu, and Yu (2015), the proposed model in this paper

give a better prediction.

Horizontal displacements

Fig. 11 plots the predicted horizontal displacements corresponding to inclinometer I2 by the proposed model with different considerations of S_t. All cases give reasonable results and the same trend. Again, higher S_t (that of $2S_t$) results in higher horizontal displacement, and the model with calibrated parameters (that of S_t) generally better captured the long-term horizontal displacement behavior of embankment. The predictions are more closing to the experimental data at 3201 days after the construction than Yin, Xu, and Yu (2015). Note that the differences between predictions and measurements for the horizontal displacement below 13 m are probably due to the constant Poisson's ratio used in the simulations or/and no consideration of small strain stiffness in the current model which needs further studies.

Excess pore pressure

Fig. 12 shows the model predictions with different considerations of S_t for excess pore pressure in the foundation soil under the centerline at a depth of 2 m, 5.5 m and 9 m respectively. For all predictions, the excess pore pressure is increasing during the procedure of construction. However, the excess pore pressure at the depth of 2 m decreases directly after fill placement (Fig. 12a). Meanwhile, the excess pore pressures at the depth of 5.5 m and 9 m increase continuously for some certain days after fill placement (Fig. 12b and Fig. 12c), and then dissipate gradually with time. The comparisons between different S_t imply that the influence of consideration of creep degradation on the evolution of excess pore pressure is unneglectable, which coincide with the reports by Leroueil (1988), Yin, Xu, and Yu (2015) and Kabbaj, Tavenas, and Leroueil (1988), .

4.2 Gloucester test fill

Finite element model

Gloucester test embankment is an unreinforced test embankment on a soft clay deposit. The details of Gloucester case history are given by Lo, Bozozuk, and Law (1976), Hinchberger and Rowe (1998, 2005). The domain to be analyzed (under plane strain conditions) has an extent of 40 m in the horizontal direction from the symmetry axis and 20.2 m in the vertical direction as used in Hinchberger and Rowe (1998). The lateral boundaries are fixed horizontally, and the bottom boundary is fixed in both directions (see Fig. 13). At 20.2 m depth, a rough rigid permeable boundary was assumed. The finite element mesh is constituted of 2922 6-noded triangular elements resulting in 5975 nodes. The sand fill of the embankment ~~fill~~ was modeled as a simple linear elastic–perfectly plastic Mohr Coulomb material, and values of model parameters based on Hinchberger and Rowe (2005) are summarized in Table 3. The test fill was constructed on the floor of the 1.2 m excavation up to the original ground surface for 25 days. The net height (2.4 m) of the embankment was then finished in the following one week. The real construction procedures of the embankment were simulated fully in the modeling.

Parameters of foundation clays

For foundation soils, Fig. 14 shows the distribution with depth for preconsolidation pressure, vertical permeability, and Atterberg limits. The model parameters were chosen based on the extensive laboratory tests and field investigations. As shown in Fig. 14a, parameter POP were measured by subtracting self-weight (unit weight γ=16.8 kN/m^3 for all the soils in the domain area according to Lo, Bozozuk, and Law (1976)) from maximum values of preconsolidation pressure. Considering that the samples utilized in laboratory test are more or less disturbed, the maximum envelope curve of preconsolidation pressure are assumed from less disturbed samples. The permeability is determined from Fig. 14b and that reported in Hinchberger and Rowe (1998, 2005). The liquid limit w_L is determined from Fig. 3c, based on which the intrinsic compression index is estimated from the correlation λ_L=0.007·(w_L-10)/ln(10) by Skempton and Jones (1944). The swelling index κ = 0.025 is assumed for all layers and S_t = 20 for all the clays in the modeling

are utilized according to the index properties investigation by Hinchberger and Rowe (2005). ~~The swelling index κ is assumed as 1/10 of the compression index. S_t = 20 for all the clays in the modeling is utilized according to the index properties investigation by Hinchberger and Rowe (2005).~~

Note that the key state variable $C_{\alpha e}$ in the model is determined from the liquid limit w_L which was not richly investigated and documented (only 5 measurements), two group values are adopted noted as $w_{L\text{-min}}$ and $w_{L\text{-max}}$ as shown in Fig. 14c. Then, two groups of λ_L and κ were used for simulations accordingly. A long-term oedometer test under the load increment from 38.5 kPa to 80.8 kPa on a sample from 2.4 m depth was simulated to calibrate the value of ξ, from which $\xi = 12$ and $\xi = 4$ were best fitted for $w_{L\text{-min}}$ and $w_{L\text{-max}}$ respectively, as shown in Fig. 15.

All input parameters are summarized in Table 5 with some of them reported in Hinchberger and Rowe (1998, 2005).

Settlements

In Fig. 16, the measurement of settlement versus time is compared with calculated results using different liquid limits. The calculated settlement below centerline of the embankment is less than measured settlement at all depth when w_L equals to the minimum value. The calculated settlement exceeds measured values when the maximum w_L is used in the analysis. In the other words, the measured settlement rightly lies in the middle of the two simulations with maximum and minimum w_L, which demonstrates a good applicability of the proposed model using liquid limit to the embankment on soft structured clays.

Horizontal displacements

Fig. 17 presents the horizontal displacements at the toe of the embankment using the two values of w_L at the time of just after and 3.75 years after the construction. At the end of

construction, the predicted horizontal displacements with maximum and minimum w_L are slightly different, and both of them are close to the measurements. At the 3.75 years after the construction, the predicted horizontal displacements between 2.0 and 4.0 m are a little bigger than measurements. The measured displacements between 4.0 and 7.5 m below the original ground level are lying in the middle of the two simulations with maximum and minimum w_L. In general, the model gives a reasonable prediction comparing to the measurements.

5. Conclusions

Phenomena of creep degradation were first investigated based on available test data on both intact and reconstituted ~~natural~~ Marine deposited clay samples. The contributions of the inter-particle bonding and debonding for Marine deposited structured clays to creep coefficient $C_{\alpha e}$ were analyzed and a structure parameter (ρ) based on creep was defined. Then, this structure parameter with destructuration to creep is incorporated into an anisotropic elastic viscoplastic model to describe the creep degradation strightforwordly. The correlation between creep index, soil structure, and liquid limit was established, based on which the liquid limit was adopted as input parameter. Comparing to Modified Cam-Clay model, three additional parameters (soil sensitivity, liquid limit, and a destructuration parameter) are needed for the proposed model.

The model was implemented into a 3D Finite Element code adopting Newton-Raphson algorithm, by which the coupled consolidation analysis can be carried out. The predictive ability on creep degradation of the proposed model was first validated by simulating laboratory tests on both reconstituted and intact samples of Murro clay. Then, the well documented Murro test embankment was simulated by the proposed model with the creep parameter determined by the liquid limit for the validation and application. Different assumed values of soil sensitivity were used to simulate the embankment, based on which the importance of soil sensitivity on the creep degradation during long-term behavior of embankment on ~~soft~~ marine sensitive clays was highlighted.

The Gloucester test fill was further simulated by the proposed model. A band of liquid limit value based on available measurements was examined through simulations compared to field measurements. The applicability of the proposed model with creep degradation was validated for embankment on ~~soft~~ marine structured clays.

Acknowledgement

We acknowledge with gratitude the financial support provided by the National Natural Science Foundation of China (Grant No. 41502271, 51808407), 111 project (B14021), and State Key Laboratory for GeoMchanics and Deep Underground Engineering, China University of Mining & Technology (SKLGDUEK1714).

References

Araújo, G. L. S., E. M. Palmeira, and Í. L. Macêdo. 2012. Comparisons between predicted and observed behaviour of a geosynthetic reinforced abutment on soft soil. *Engineering Geology* 147:101-113.

Bergado, D. T., and C. Teerawattanasuk. 2008. 2D and 3D numerical simulations of reinforced embankments on soft ground. *Geotextiles & Geomembranes* 26 (1): 39-55.

Borges, J. L., and D. O.Marques. 2011. Geosynthetic-reinforced and jet grout column-supported embankments on soft soils: Numerical analysis and parametric study. *Computers and Geotechnics* 38 (7): 883-896.

Chai, J., Y. Igaya, T. Hino and J. Carter. 2013. Finite element simulation of an embankment on soft clay - case study. *Computers and Geotechnics* 48 (1): 117-126.

Dai, Z. H., B. L. Chen, and Z. Z. Qin. 2017. Three-dimensional nonlinear numerical analysis of consolidation of soft ground improved by sand columns under a freeway embankment in shallow sea: case study. *International Journal of Geomechanics* 17 (8). doi:10.1061/(ASCE)GM.1943-5622.0000906 (2017)

D'Ignazio, M., T. T. Lansivaara, and H. P. Jostad. 2017. Failure in anisotropic sensitive clays: a finite element study of Pernio failure test. *Canadian Geotechnical Journal* 54 (7): 1013-1033.

Hinchberger, S. D., and G. F. Qu. 2009. Viscoplastic constitutive approach for rate-sensitive structured clays. *Canadian Geotechnical Journal* 46 (6): 609-626.

Hinchberger, S. D., and R. Rowe. 1998. Modelling the rate-sensitive characteristics of the Gloucester foundation soil. *Canadian Geotechnical Journal* 35 (5): 769-789.

Hinchberger, S.D., and R. Rowe. 2005. Evaluation of the predictive ability of two elastic-viscoplastic constitutive models. *Canadian Geotechnical Journal* 42 (6): 1675-1694.

Huang, W., S. Fityus, D. Bishop, D. Smith, and D. Sheng. 2006. Finite-Element Parametric Study of the Consolidation Behavior of a Trial Embankment on Soft Clay. *International Journal of Geomechanics* 6(5): 328-341.

Indraratna, B., and A. Balasubramaniam. 1997. Analysis of settlement and lateral deformation of soft clay foundation beneath two full-scale embankments. *International Journal for Numerical and Analytical Methods in Geomechanics* 21: 599-618

Jamsawang, P., E. Phongphinittana, P. Voottipruex, D. T. Bergado, and P. Jongpradist. 2018. Comparative

performances of two- and three-dimensional analyses of soil-cement mixing columns under an embankment load. Marine Georesources & Geotechnology, 1-18. doi:10.1080/1064119X.2018.1504261

Jin, Y. F., Z. Y. Yin, Y. Riou, and P. Y. Hicher. 2017. Identifying creep and destructuration related soil parameters by optimization methods. *KSCE Journal of Civil Engineering* 21(4): 1123-1134.

Kabbaj, M., F. Tavenas, and S. Leroueil. 1988. In situ and laboratory stress–strain relationships. *Geotechnique* 38 (1): 83-100.

Karim, M. R., C. T. Gnanendran, S. C. R. Lo, and J. Mak. 2010. Predicting the long-term performance of a wide embankment on soft soil using an elastic–viscoplastic model. *Canadian Geotechnical Journal* 47 (2): 244-257.

Karlsson, M., A. Emdal, and J. Dijkstra. 2016. Consequences of sample disturbance when predicting long-term settlements in soft clay. *Canadian Geotechnical Journal* 53 (12): 1965-1977.

Karstunen, M., H. Krenn, S. J. Wheeler, M. Koskinen, and R. Zentar. 2005. Effect of anisotropy and destructuration on the behavior of Murro test embankment. *International Journal of Geomechanics* 5 (2): 87-97.

Karstunen, M., C. Wiltafsky, H. Krenn, F. Scharinger,and H. F. Schweiger. 2006. Modelling the behaviour of an embankment on soft clay with different constitutive models. *International Journal for Numerical and Analytical Methods in Geomechanics* 30 (10): 953-982.

Karstunen, M., and Z. Y. Yin. 2010. Modelling time-dependent behaviour of Murro test embankment. *Geotechnique* 60 (10): 735–749.

Kelln, C., J. Sharma, D. Hughes, and J. Graham. 2009. Finite element analysis of an embankment on a soft estuarine deposit using an elastic–viscoplastic soil model. *Canadian Geotechnical Journal* 46 (3): 357-368.

Kim, Y., and S. Leroueil. 2001. Modeling the viscoplastic behaviour of clays during consolidation: application to Berthierville clay in both laboratory and field conditions. *Canadian Geotechnical Journal* 38 (3): 484-797.

Kimoto, S., and F. Oka. 2005. An elasto-viscoplastic model for clay considering destructuralization and consolidation analysis of unstable behaviour. *Soils and Foundations* 45 (2): 29-42.

Leoni, M., M. Karstunen, and P. A. Vermeer. 2008. Anisotropic creep model for soft soils. *Geotechnique*

58 (3): 215-226.

Leroueil, S. 1988. Tenth Canadian Geotechnical Colloquium: Recent developments in consolidation of natural clays. *Canadian Geotechnical Journal* 25 (1): 85-107.

Leroueil, S., M. Kabbaj, F. Tavenas, and R. Bouchard. 1985. Stress-strain-strain rate relation for the compressibility of sensitive natural clays. *Geotechnique* 35 (2): 159-180.

Lo, K. Y., M. Bozozuk, and K. T. Law. 1976. Settlement analysis of the Gloucester test fill. *Canadian Geotechnical Journal* 13 (4): 339-354

Mesri, G., and P. Godlewski. 1977. Time and stress-compressibility interrelationship. *Journal of Geotechnical and Geoenvironmental Engineering* 105 (5): 417-430.

Mitchell, J. K., K. Soga. 2005. Fundamentals of soil behavior. New York: Wiley

Müthing, N., C. Zhao, R. Hölter, and T. Schanz. 2018. Settlement prediction for an embankment on soft clay. *Computers and Geotechnics* 93: 87-103.

Nagaraj, T., and B. R .S. Murthy. 1983. Rationalization of Skempton's compressibility equation. *Geotechnique* 33 (4): 433-443.

Nunez, M. A., L. Briançon, and D. Dias. 2013. Analyses of a pile-supported embankment over soft clay: Full-scale experiment, analytical and numerical approaches. *Engineering Geology* 153 (2): 53-67.

Oka, F., T. Adachi, and Y. Okano. 1986. Two-dimensional consolidation analysis using an elasto-viscoplastic constitutive equation. *International Journal for Numerical and Analytical Methods in Geomechanics* 10 (1): 1-16

Panayides, S., M. Rouainia, and D. M. Wood. 2012. Influence of degradation of structure on the behaviour of a full-scale embankment. *Canadian Geotechnical Journal* 49 (3): 344-356.

Perzyna, P. 1966. Fundamental problems in viscoplasticity. *Advances in Applied Mechanics* 9 (2): 243-377.

Rezania, M., M. Bagheri, M. M. Nezhad, and N. Sivasithamparam. 2017. Creep analysis of an earth embankment on soft soil deposit with and without PVD improvement. *Geotextiles and Geomembranes* 45: 537-547

Rocchi, G., M. Fontana, and M. Da Prat. 2003. Modelling of natural soft clay destruction processes using viscoplasticity theory. *Geotechnique* 53 (8): 729–745.

Roscoe, K. H., and J. B. Burland. 1968. On the generalized stress-strain behaviour of wet clay. Cambridge

University Press: Cambridge

Rowe, R .K., and A. L. LI. 2002. Behaviour of reinforced embankments on soft rate-sensitive soils. *Geotechnique* 52 (1): 29-40.

Rowe, R.K., and K.W. Liu. 2015. Three-dimensional finite element modelling of a full-scale geosyntheti. *Canadian Geotechnical Journal* 52 (12): 2041-2054.

Skempton, A. W., and O. T. Jones. 1944. Notes on the compressibility of clays. *Quarterly Journal of the Geological Society* 100 (1-4): 119-135.

Tanchaisawat, T., D. T. Bergado, and P. Voottipruex. 2008. Numerical simulation and sensitivity analyses of full-scale test embankment with reinforced lightweight geomaterials on soft Bangkok clay. *Geotextiles and Geomembranes* 26 (6): 498-511.

Vermeer, P. A., and H. P. Neher. 1999. A Soft Soil Model that Accounts for Creep. Proceeding in Plaxis Symposium "Beyond 2000 in Computational Geotechnics". Amsterdam, 249-262.

Yin, J. H. 1999. Non-linear creep of soils in oedometer tests. *Geotechnique* 49 (5): 699-707.

Yin, J. H. and J. Graham. 1989. Viscous elastic plastic modelling of one dimensional time dependent bahavior of clays. *Canadian Geotechnical Journal* 26 (2): 199-209.

Yin, J. H., J. G. Zhu, and J. Graham. 2002. A new elastic viscoplastic model for time-dependent behaviour of normally and overconsolidated clays: theory and verification. *Canadian Geotechnical Journal* 39(1): 157-173.

Yin, Z. Y., C. S. Chang, M. Karstunen, and P. Y. Hicher. 2010. An anisotropic elastic viscoplastic model for soft soils. *International Journal of Solids and Structures* 47 (5): 665-677.

Yin, Z.Y., M. Hattab, and P. Y. Hicher. 2011. Multiscale modeling of a sensitive marine clay. *International Journal for Numerical and Analytical Methods in Geomechanics* 35 (15): 1682-1702.

Yin, Z.Y., Y. F. Jin, H. W. Huang, and S. L. Shen. 2016. Evolutionary polynomial regression based modelling of clay compressibility using an enhanced hybrid real-coded genetic algorithm. *Engineering Geology* 210 (5): 158-167.

Yin, Z. Y., M. Karstunen, C. S. Chang, M. Koskinen, and M. Lojander. 2011. Modeling time-dependent behavior of soft sensitive clay. *Journal of Geotechnical and Geoenvironmental Engineering* 137 (11): 1103-1113.

Yin, Z.Y., and J. H. Wang. 2012. A one-dimensional strain-rate based model for soft structured clays. *Science China Technological Sciences* 55(1): 90-100.

Yin, Z. Y., Q. Xu, and C. Yu. 2015. Elastic Viscoplastic Modeling for Natural Soft Clays Considering Nonlinear Creep. *International Journal of Geomechanics* 15 (5): A6014001

Yin, Z. Y., Q. Y. Zhu, and D. M. Zhang. 2017. Comparison of two creep degradation modeling approaches for soft structured soils. *Acta Geotechnica* 12 (6): 1395-1413.

Zhu, J. G., and J. H. Yin. 2012. Elastic viscoplastic modelling of consolidation behaviour of a test embankment treated with PVD, *The 3rd Asian Regional Conference on Geosynthetics*, Seoul, Korea, 298-305.

Zhu, Q.Y., Z. Y. Yin, P. Y. Hicher,.and S. L. Shen. 2016. Non-linearity of one-dimensional creep characteristics of soft clays. *Acta Geotechnica* 11 (4): 887-900.

Zhu, Q.Y., Z. Y. Yin, D. M. Zhang, and H. W. Huang. 2017. Numerical modeling of creep degradation of natural soft clays under one-dimensional condition. *KSCE Journal of Civil Engineering* 21 (5): 1668-1678.

Appendix: Brief description of ANICREEP model

Yin et al. (2010) have proposed an anisotropic elastic viscoplastic model for soft soils, in which the strain-rate dependency parameters ($\dot{\varepsilon}_v^r, \beta$) or creep coefficient ($C_{\alpha e}$) can be alternatively used. According to Yin et al. (2010), the basic elastic viscoplastic equations are listed:

[A1] $$\dot{\varepsilon}_{ij} = \dot{\varepsilon}_{ij}^{e} + \dot{\varepsilon}_{ij}^{vp}$$

[A2] $$\dot{\varepsilon}_{ij}^{vp} = \mu \left(\frac{p_m^d}{p_m^r} \right)^{\beta} \frac{\partial f_c}{\partial \sigma'_{ij}}$$

[A3] $$f_r = \frac{\frac{3}{2}\left(\sigma_d'^r - p'^r \alpha_d\right) : \left(\sigma_d'^r - p'^r \alpha_d\right)}{\left(M^2 - \frac{3}{2}\alpha_d : \alpha_d\right) p'^r} + p'^r - p_m^r = 0$$

[A4] $$d\alpha_d = \omega \left[\left(\frac{3\sigma_d}{4p'} - \alpha_d \right) \left\langle d\varepsilon_v^{vp} \right\rangle + \omega_d \left(\frac{\sigma_d}{3p'} - \alpha_d \right) d\varepsilon_d^{vp} \right]$$

[A5] $$dp_m^r = p_m^r \left(\frac{1+e_0}{\lambda_i - \kappa} \right) d\varepsilon_v^{vp}$$

where $\dot{\varepsilon}_{ij}$ means the total strain rate tensor in the (*i,j*) component, and the superscripts *e* and *vp* denote the elastic and the viscoplastic components respectively. The elastic behavior in the proposed model is assumed to be isotropic similar to the MCC model. $p^{\mathrm{d}}_{\mathrm{m}}$ is the size of current loading surface. $p^{\mathrm{r}}_{\mathrm{m}}$ is the size of reference surface. The initial reference preconsolidation pressure $\sigma_{p0}'^r$ measured from oedometer test can be used to calculate the initial size $p^{\mathrm{r}}_{\mathrm{m}}$ by following the Eq. [A9].

Based on the conventional oedometer test for the convenience in this paper, the fluidity μ and the strain-rate coefficient β in Eq. [A2] are expressed as follows, if the creep coefficient is adopted:

[A6] $$\mu = \frac{C_{\alpha e}}{(1+e_0)\tau} \frac{\left(M_c^2 - \alpha_{K0}^2\right)}{\left(M_c^2 - \eta_{K0}^2\right)} \quad \text{and} \quad \beta = \frac{\lambda_i - \kappa}{C_{\alpha e0}(R)}$$

The initial surface inclination α_0 and values of parameters related to anisotropy are calculated by

[A7] $$\alpha_0 = \alpha_{K0} = \eta_{K0} - \frac{M_c^2 - \eta_{K0}^2}{3} \quad \text{with} \quad \eta_{K0} = \frac{3M_c}{6 - M_c} \quad \text{and} \quad K_0 = \frac{6 - 2M_c}{6 + M_c}$$

[A8] $$\omega = \frac{1 + e_0}{(\lambda_i - \kappa)} \ln \frac{10M_c^2 - 2\alpha_{K0}\omega_d}{M_c^2 - 2\alpha_{K0}\omega_d} \quad \text{with} \quad \omega_d = \frac{3\left(4M_c^2 - 4\eta_{K0}^2 - 3\eta_{K0}\right)}{8\left(\eta_{K0}^2 + 2\eta_{K0} - M_c^2\right)}$$

The initial size of reference surface p^r_{m0} is calculated by the preconsolidation pressure as follows,

[A9] $$p_{m0}^r = \left\{ \frac{\left[3 - 3K_0 - \alpha_{K0}(1 + 2K_0)\right]^2}{3\left(M_c^2 - \alpha_{K0}^2\right)(1 + 2K_0)} + \frac{(1 + 2K_0)}{3} \right\} \sigma'^r_{p0}$$

The slope of critical state line M is expressed as follows:

[A10] $$M = M_c \left[\frac{2c^4}{1 + c^4 + (1 - c^4)\sin 3\theta} \right]^{\frac{1}{4}}$$

where $c = (3 - \sin\phi_c)/(3 + \sin\phi_c)$ according to Mohr-Coulomb yield criterion (ϕ_c is the friction angle); $\frac{-\pi}{6} \le \theta = \frac{1}{3}\sin^{-1}\left(\frac{-3\sqrt{3}\bar{J}_3}{2\bar{J}_2^{3/2}}\right) \le \frac{\pi}{6}$ using $\bar{J}_2 = \frac{1}{2}\bar{s}_{ij} : \bar{s}_{ij}$, $\bar{J}_3 = \frac{1}{3}\bar{s}_{ij}\bar{s}_{jk}\bar{s}_{ki}$ with $\bar{s}_{ij} = \sigma_d - p'\alpha_d$.

The scalar value of as can be difined as :

[A11] $$\alpha_s = \sqrt{3/2(\alpha_d : \alpha_d)}$$

During consolidation coupled analyses, the permeability k varies with void ratio e:

[A12] $$k = k_0 10^{(e - e_0)/c_k}$$

The definitions of material constants and state variables needed for the model are summarized in Table A1 with their determination.

Table A1. State parameters and soil constants of elastic viscoplastic model

Group	Parameter	Definition	Determination
Standard model parameter	σ'^r_{p0}	Initial reference pre-consolidation pressure	From a select oedometer test
	e_0	Initial void ratio	From oedometer test

	υ	Poisson's ratio	From initial stress-strain curve (typically 0.15-0.35)
	κ	Swelling index	From compression test
	λ_L	Intrinsic compression index	From compression test
	M	Slope of the critical state line	From drained or undrained triaxial shear test
Viscosity parameter	$C_{\alpha e}$	Secondary compression coefficient or creep index	From oedometer test
Hydraulic parameter	k_{v0}, k_{h0}	Initial permeability	From oedometer test
	c_k	Permeability coefficient	From oedometer test

Tables

Table 1. Parameters of EVP model for the creep tests on Murro clay

υ	λ_L	κ	e_0	M_c	w_L/%	σ'^r_{p0} /kPa	S_t	ξ	k (m/h)
0.3	0.22	0.041	2.3	1.65	70	28	7	7	4×10^{-5}

Table 2. Average values for physical properties of Murro clay

Depth/m	w / %	I_p	γ / kN/m^3	e_0	S_t
0.0-1.6	56.8	38	16.1	1.57	3.5
1.6-3.0	64.1	48	15.7	1.81	7
3.0-6.7	91.6	66	14.4	2.45	7
6.7-10.0	79.5	51	15.2	2.16	7
10.0-15.0	67.6	49	15.7	1.76	5
15.0-23.0	58.3	31	16.2	1.53	7

Table 3. Mohr Coulomb model parameters for embankment fill

	Young's modulus E / kN/m^2	Poisson's ratio υ'	Unit weight γ / kN/m^3	Cohesion c / kN/m^2	Critical state friction angle ϕ'_c	Dilation angle ψ
Murro	40000	0.35	19.6	2	40^o	0^o
Gloucester	40000	0.35	18.4	2	36^o	0^o

Table 4. EVP model parameters for subsoil of Murro embankment

Depth/m	γ/kN/m^3	e_0	M_c	K_0	κ	λ_L	υ	w_L/%
0.0-1.6	16.1	1.57	1.7	1.25	0.01	0.18	0.3	45
1.6-3.0	15.7	1.81	1.7	0.34	0.024	0.18	0.3	60
3.0-6.7	14.4	2.45	1.65	0.35	0.041	0.25	0.3	70
6.7-10.0	15.2	2.16	1.5	0.4	0.024	0.21	0.3	90
10.0-15.0	15.7	1.76	1.45	0.42	0.024	0.21	0.3	60
15.0-23.0	16.2	1.53	1.4	0.43	0.02	0.15	0.3	60

Depth/m	*POP*/kPa	ξ	k_{v0}/m/h	k_{h0}/m/h	c_k
0.0-1.6	100	7	6.5×10^{-4}	8.3×10^{-4}	0.43
1.6-3.0	22	7	2.0×10^{-5}	2.6×10^{-5}	0.65
3.0-6.7	22	7	1.6×10^{-5}	2.2×10^{-5}	0.69
6.7-10.0	22	7	1.0×10^{-5}	1.4×10^{-5}	0.49
10.0-15.0	35	7	5.4×10^{-6}	7.2×10^{-6}	0.44
15.0-23.0	40	7	2.2×10^{-6}	2.9×10^{-6}	0.45

Table 5. EVP model parameters for subsoil of Gloucester embankment

Depth/m	e_0	M_c	K_0	κ	λ_L	υ	$w_{L\text{-}min}$/%	$w_{L\text{-}max}$/%
0.0-2.0	1.8	0.9	1.0	0.025	0.091	0.3	49	59
2.0-5.2	1.8	0.9	0.75	0.025	0.091	0.3	49	59
5.2-7.2	1.8	0.9	0.75	0.025	0.137	0.3	55	65
7.2-13.4	2.4	0.9	0.75	0.025	0.103	0.3	47	57
13.4-20.2	1.8	0.9	0.75	0.025	0.112	0.3	44	54

Depth/m	*POP*/kPa	S_t	$\xi(w_{L\text{-}min})$	$\xi(w_{L\text{-}max})$	k_{v0}/m/h	k_h/k_v	c_k
0.0-2.0	55	20	12	4	7.5×10^{-6}	1.25	0.25
2.0-5.2	30	20	12	4	5.2×10^{-6}	1.25	0.25
5.2-7.2	60	20	12	4	3.6×10^{-6}	1.25	0.5
7.2-13.4	70	20	12	4	3.6×10^{-6}	1.25	0.25
13.4-20.2	70	20	12	4	5.2×10^{-6}	1.25	0.25

Figure captions

Fig. 1 Illustration of creep coefficient versus void ratio in double logarithmic scale for reconstituted clays as proposed by Yin, Xu, and Yu (2015)

Fig. 2 Illustration creep degradation: (a) definition of the amount of inter-particle bonds; (b) evolution of creep coefficient with vertical stress for both intact and reconstituted clay; (c) definition of the amount of creep degradation

Fig. 3 Illustrations of model principle in p'-q plane

Fig. 4 Correlation between ~~soil density~~ void ratio related parameters and liquid limit: (a) $C_{\alpha eL}$-w_L; (b) m- w_L; (c) variation of m for Vanttila clay; (d) ρ_0/χ_0-w_L

Fig. 5 Flow chart for the time integration algorithm of Newton Raphson

Fig. 6 Modeling of creep degradation on Murro clay: (a) determination of parameters from oedometer tests; (b) comparisons of predicted and measured settlement curve for intact clay; (c) comparisons of predicted and measured settlement curve for reconstituted clay; (d) comparison of predicted and measured creep coefficient for both intact and reconstituted clay

Fig. 7 Test simulations for oedometer CRS tests: (a) CRS tests with different strain rate; (b) CRS tests with different S_t; (c) CRS tests with different destructuration rate parameter

Fig. 8 Test simulations for triaxial undrained creep tests: (a) ε_a-log$t$ with different S_t; (b) p'-log$t$ with different S_t

Fig. 9 Finite element model for Murro test embankment.

Fig. 10 Settlements: (a) underneath the embankment at centerline, (b) underneath embankment 5m from centerline

Fig. 11 Horizontal displacements at I2: (a) 754 days after construction; (b) 3201 days after construction

Fig. 12 Excess pore pressures: (a) U2-2m depth under centerline; (b) U4-5.5m depth under centerline; (c) U6-9 m depth under centerline

Fig. 13 Finite element model for Gloucester test fill

Fig. 14 Determination of model input parameters: (a) preconsolidation pressure; (b): hydraulic conductivity; (c) Atterberg limts

Fig. 15 Comparison between simulations and experimental results for two long term consolidation tests.

Fig. 16 Settlements predicted by using two values of w_L; (a) S1-1.8m depth under centerline; (b) U2-2.2m depth under centerline; (c) U3-5 m depth under centerline

Fig. 17 Horizontal displacements at embankment toe of the Gloucester test embankment predicted by using two values of w_L

Figures

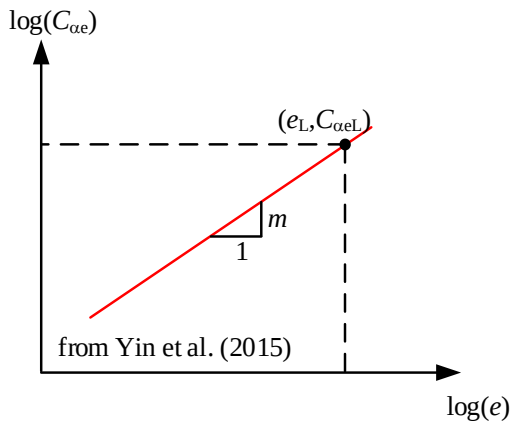

Fig. 1

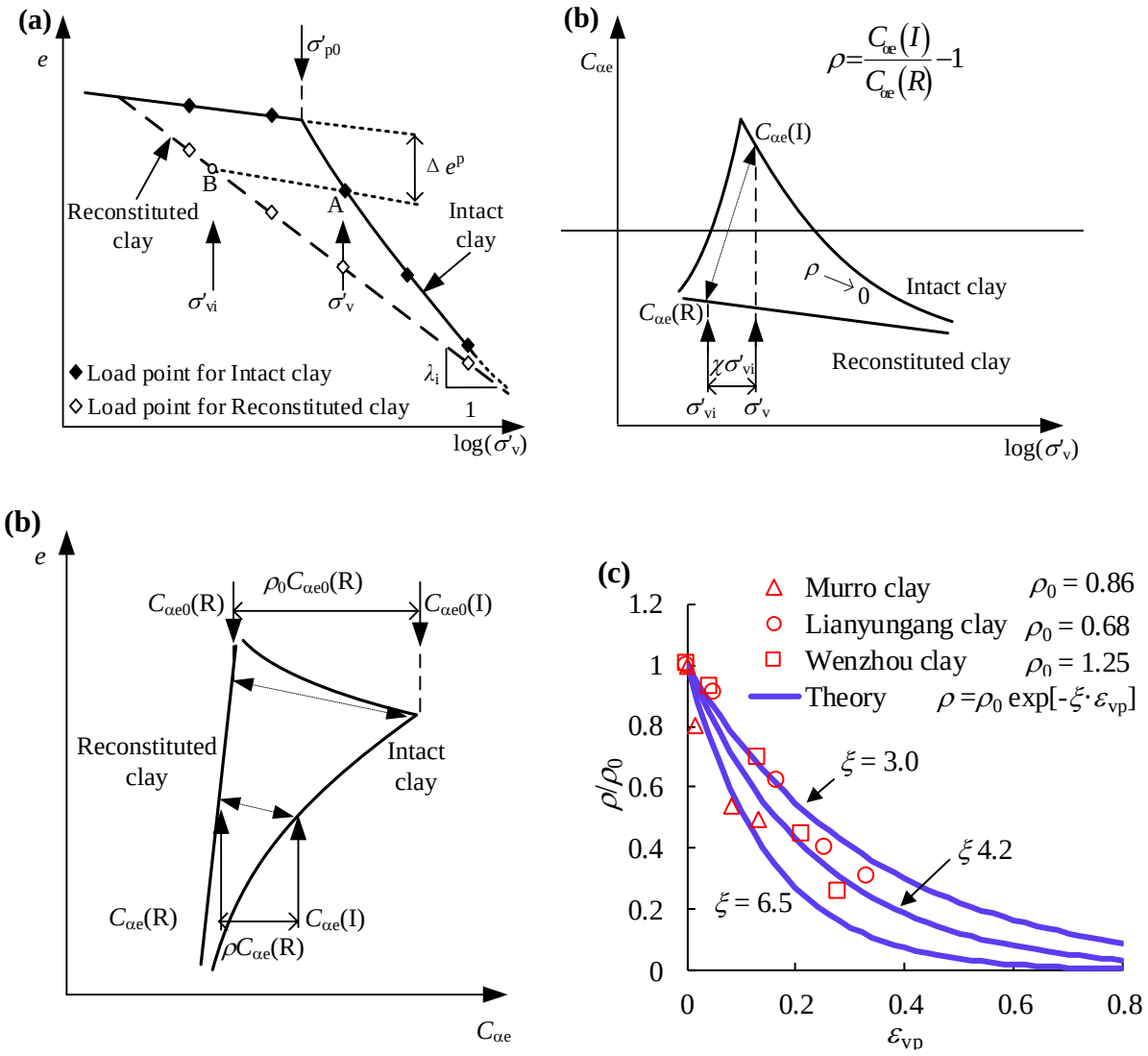
(a)
e
σ'p0
Δ ep
B
A
Reconstituted clay
Intact clay
σ'vi
σ'v
Load point for Intact clay
Load point for Reconstituted clay
λi
1
log(σ'v)
(b)
Cαe
ρ=Cαe(I)/Cαe(R)−1
Cαe(I)
ρ → 0
Intact clay
Cαe(R)
Reconstituted clay
χσ'vi
σ'vi
σ'v
log(σ'v)
(b)
e
Cαe0(R)
ρ0Cαe0(R)
Cαe0(I)
Reconstituted clay
Intact clay
Cαe(R)
Cαe(I)
ρCαe(R)
Cαe
(c)
Murro clay ρ0 = 0.86
Lianyungang clay ρ0 = 0.68
Wenzhou clay ρ0 = 1.25
Theory ρ =ρ0 exp[-ξ·εvp]
ξ = 3.0
ξ 4.2
ξ = 6.5
ρ/ρ0
1.2
1
0.8
0.6
0.4
0.2
0
0
0.2
0.4
0.6
0.8
εvp

Fig. 2

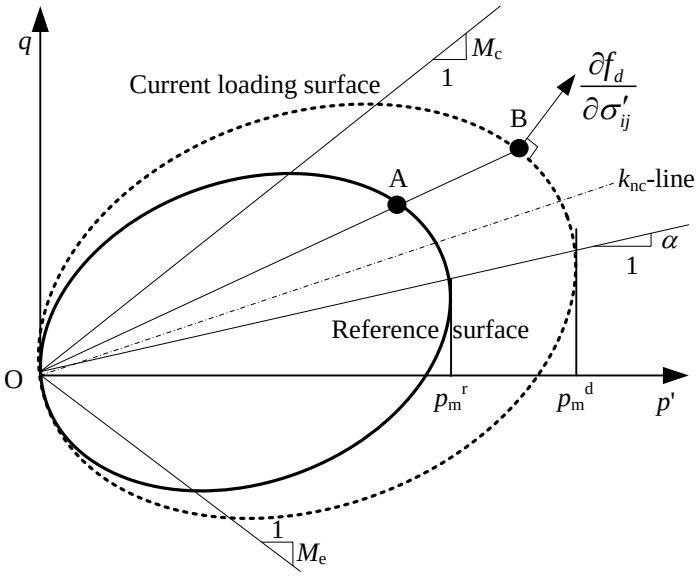
q
Current loading surface
M_c
1
$\frac{\partial f_d}{\partial \sigma'_{ij}}$
B
A
k_{nc}-line
α
1
Reference surface
O
p_m^r
p_m^d
p'
1
M_e

Fig. 3

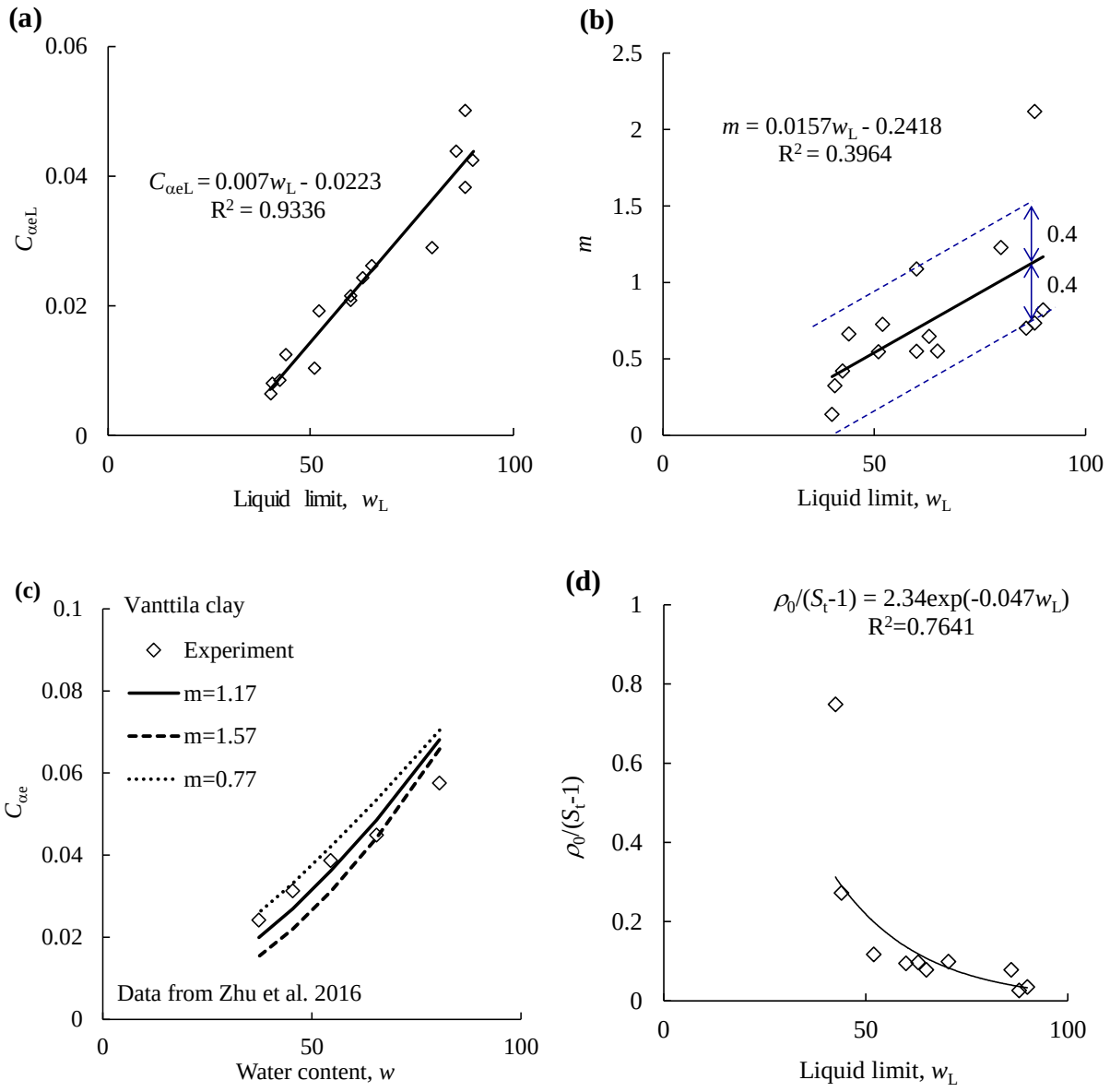
(a)
0.06
0.04
0.02
0
$C_{\alpha eL}$
$C_{\alpha eL}$ = 0.007w_L - 0.0223
R² = 0.9336
0
50
100
Liquid limit, w_L
(b)
2.5
2
1.5
1
0.5
0
m
m = 0.0157w_L - 0.2418
R² = 0.3964
0.4
0.4
0
50
100
Liquid limit, w_L
(c)
0.1
0.08
0.06
0.04
0.02
0
$C_{\alpha e}$
Vanttila clay
Experiment
m=1.17
m=1.57
m=0.77
Data from Zhu et al. 2016
0
50
100
Water content, w
(d)
1
0.8
0.6
0.4
0.2
0
$\rho_0/(S_t\text{-}1)$
$\rho_0/(S_t\text{-}1)$ = 2.34exp(-0.047w_L)
R²=0.7641
0
50
100
Liquid limit, w_L

Fig. 4

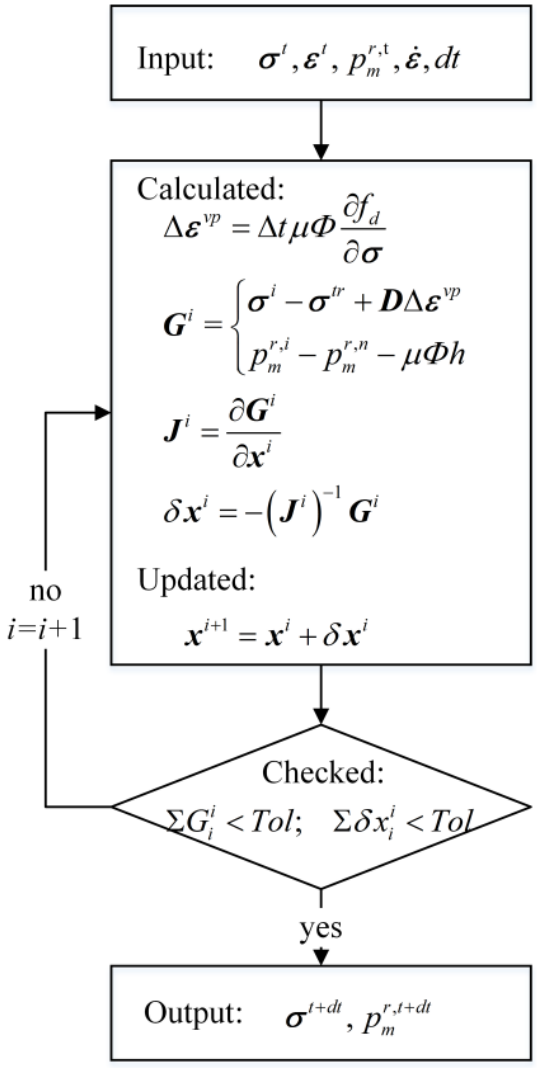
Input: $\boldsymbol{\sigma}^t, \boldsymbol{\varepsilon}^t, p_m^{r,t}, \dot{\boldsymbol{\varepsilon}}, dt$
Calculated:
$\Delta\boldsymbol{\varepsilon}^{vp} = \Delta t \mu \Phi \frac{\partial f_d}{\partial \boldsymbol{\sigma}}$
$\boldsymbol{G}^i = \begin{cases} \boldsymbol{\sigma}^i - \boldsymbol{\sigma}^{tr} + \boldsymbol{D}\Delta\boldsymbol{\varepsilon}^{vp} \\ p_m^{r,i} - p_m^{r,n} - \mu\Phi h \end{cases}$
$\boldsymbol{J}^i = \frac{\partial \boldsymbol{G}^i}{\partial \boldsymbol{x}^i}$
$\delta \boldsymbol{x}^i = -\left(\boldsymbol{J}^i\right)^{-1} \boldsymbol{G}^i$
Updated:
$\boldsymbol{x}^{i+1} = \boldsymbol{x}^i + \delta \boldsymbol{x}^i$
no
$i=i+1$
Checked:
$\Sigma G_i^i < Tol; \quad \Sigma \delta x_i^i < Tol$
yes
Output: $\boldsymbol{\sigma}^{t+dt}, p_m^{r,t+dt}$

Fig. 5

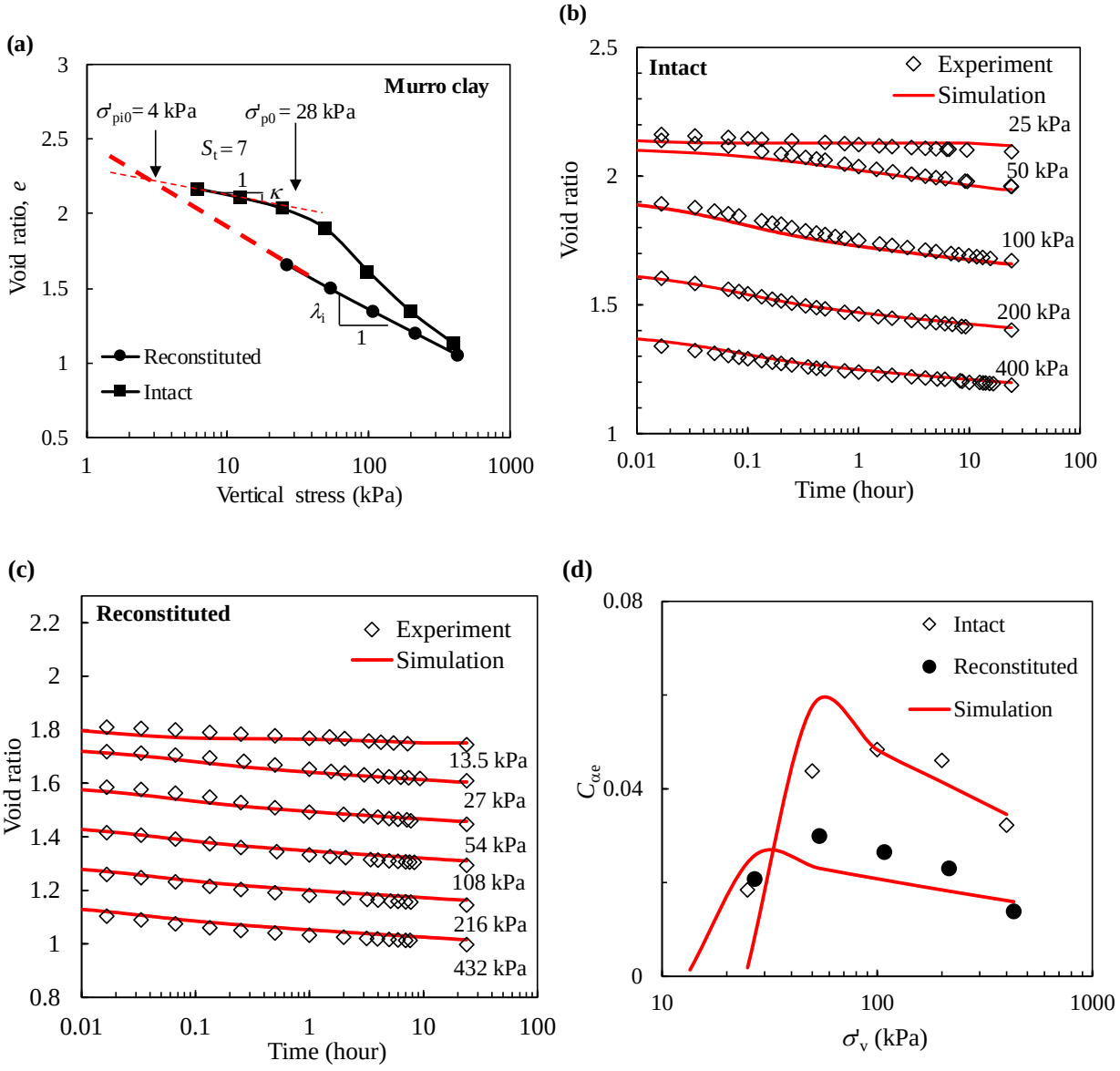
(a)
Murro clay
σ'_{pi0}= 4 kPa
σ'_{p0} = 28 kPa
S_t = 7
1
κ
λ_i
1
Reconstituted
Intact
Void ratio, e
Vertical stress (kPa)
(b)
Intact
Experiment
Simulation
25 kPa
50 kPa
100 kPa
200 kPa
400 kPa
Void ratio
Time (hour)
(c)
Reconstituted
Experiment
Simulation
13.5 kPa
27 kPa
54 kPa
108 kPa
216 kPa
432 kPa
Void ratio
Time (hour)
(d)
Intact
Reconstituted
Simulation
$C_{\alpha e}$
σ'_v (kPa)

Fig. 6

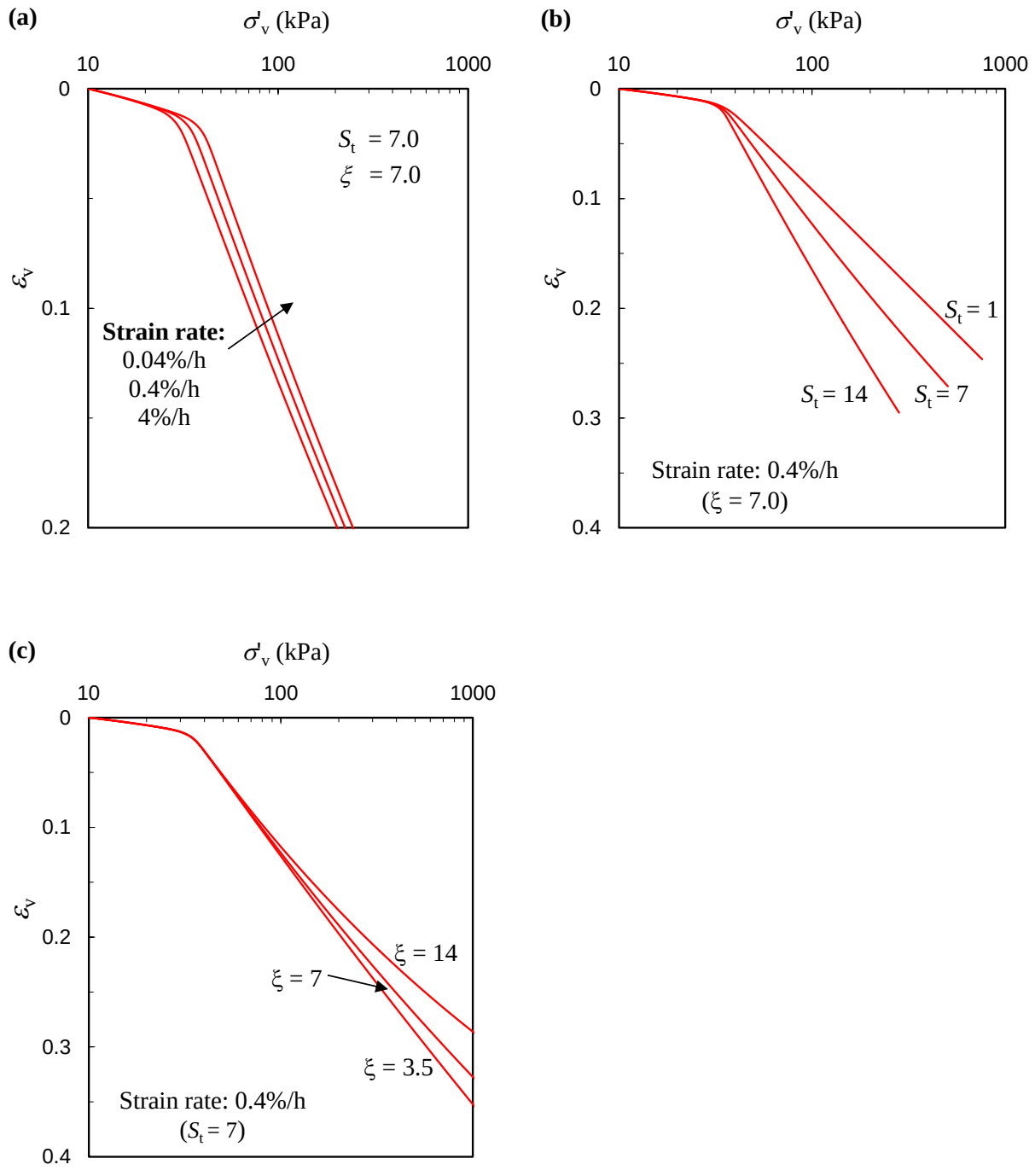
(a)
σ'v (kPa)
10
100
1000
0
0.1
0.2
εv
St = 7.0
ξ = 7.0
Strain rate:
0.04%/h
0.4%/h
4%/h
(b)
σ'v (kPa)
10
100
1000
0
0.1
0.2
0.3
0.4
εv
St = 1
St = 14
St = 7
Strain rate: 0.4%/h
(ξ = 7.0)
(c)
σ'v (kPa)
10
100
1000
0
0.1
0.2
0.3
0.4
εv
ξ = 14
ξ = 7
ξ = 3.5
Strain rate: 0.4%/h
(St = 7)

Fig. 7

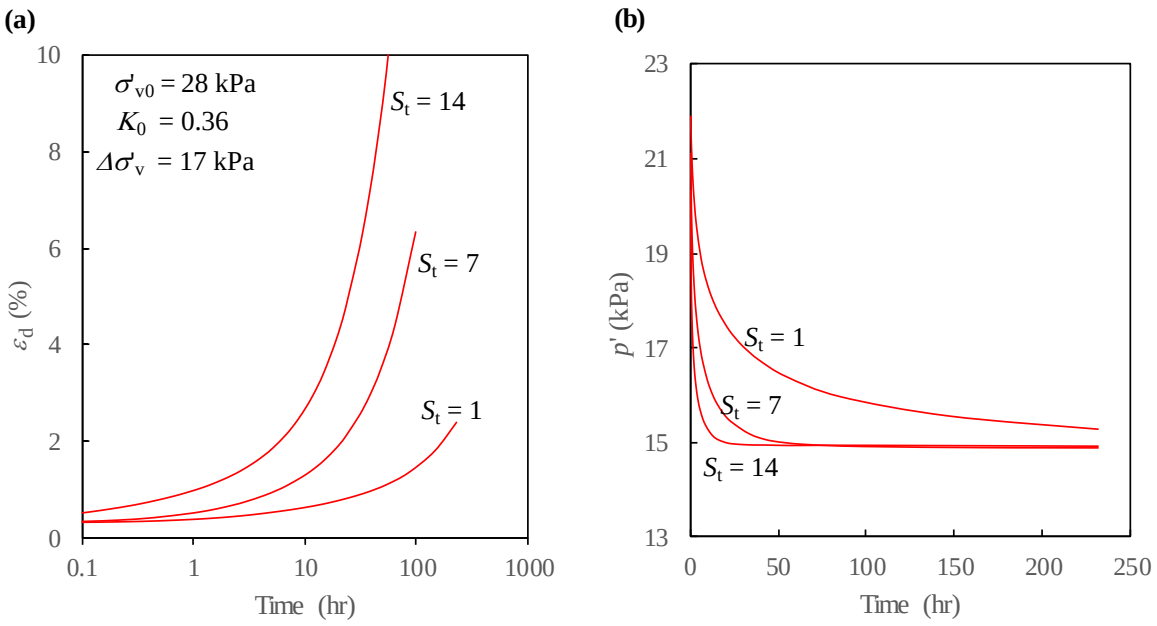
(a)
10
8
6
4
2
0
ε_d (%)
σ'_{v0} = 28 kPa
K_0 = 0.36
$\Delta\sigma'_v$ = 17 kPa
S_t = 14
S_t = 7
S_t = 1
0.1
1
10
100
1000
Time (hr)
(b)
23
21
19
17
15
13
p' (kPa)
S_t = 1
S_t = 7
S_t = 14
0
50
100
150
200
250
Time (hr)

Fig. 8

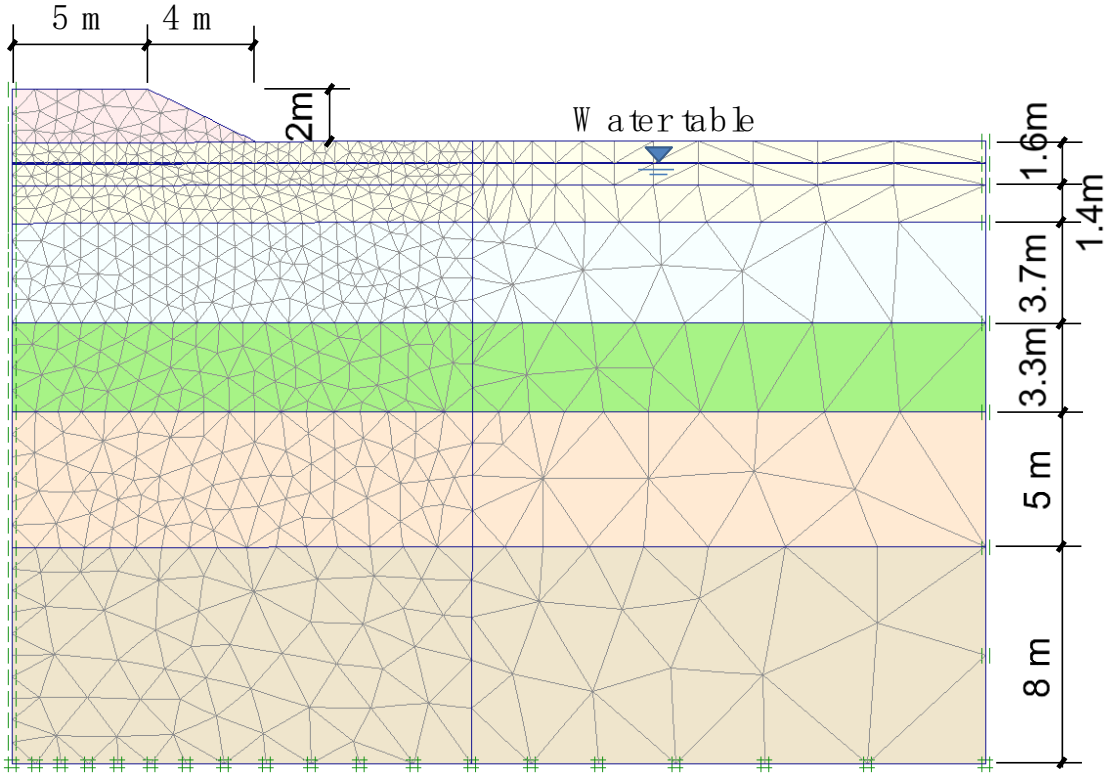

Fig. 9

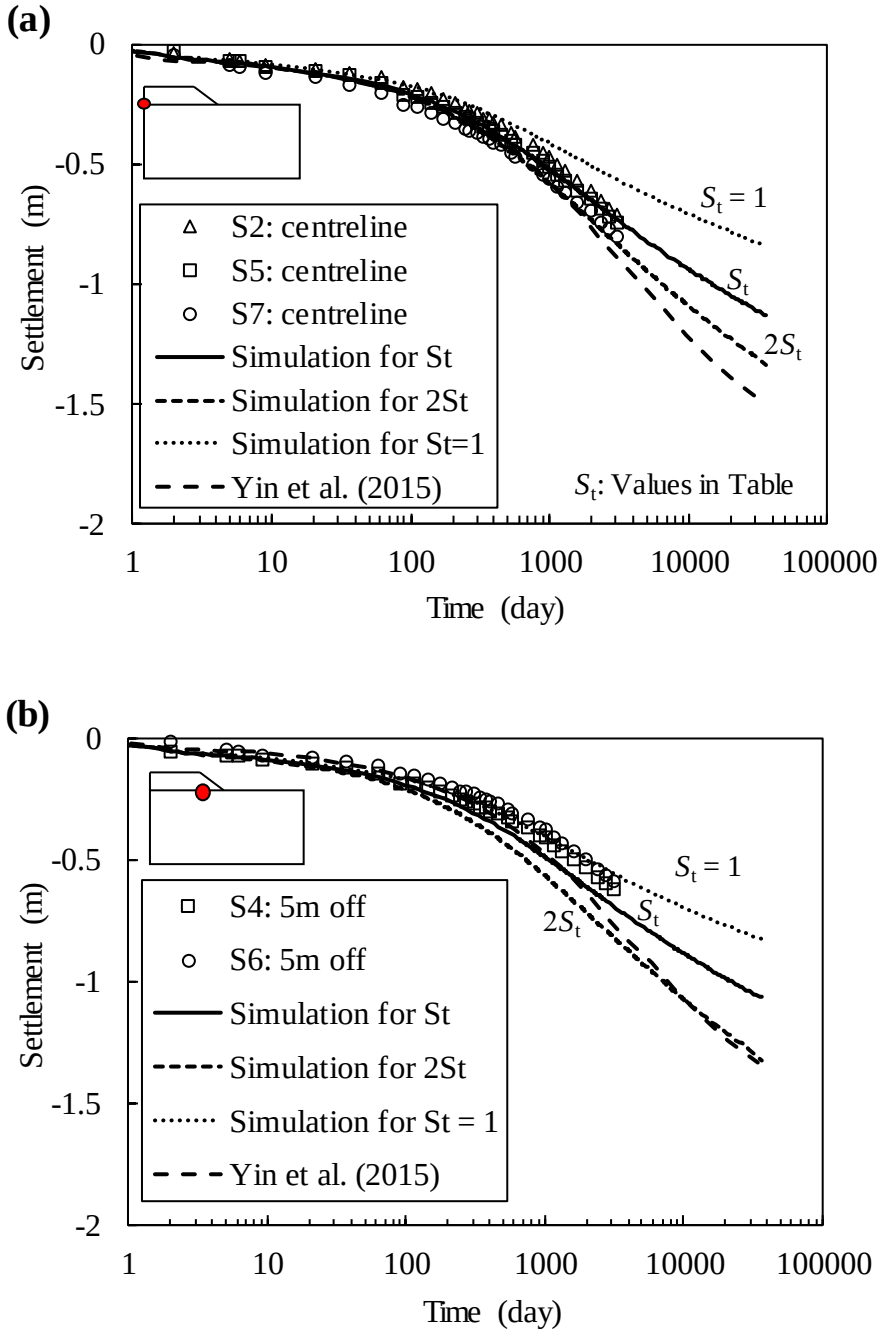
(a)
0
-0.5
-1
-1.5
-2
Settlement (m)
1
10
100
1000
10000
100000
Time (day)
S2: centreline
S5: centreline
S7: centreline
Simulation for St
Simulation for 2St
Simulation for St=1
Yin et al. (2015)
S_t: Values in Table
S_t = 1
S_t
$2S_t$
(b)
0
-0.5
-1
-1.5
-2
Settlement (m)
1
10
100
1000
10000
100000
Time (day)
S4: 5m off
S6: 5m off
Simulation for St
Simulation for 2St
Simulation for St = 1
Yin et al. (2015)
S_t = 1
S_t
$2S_t$

Fig. 10

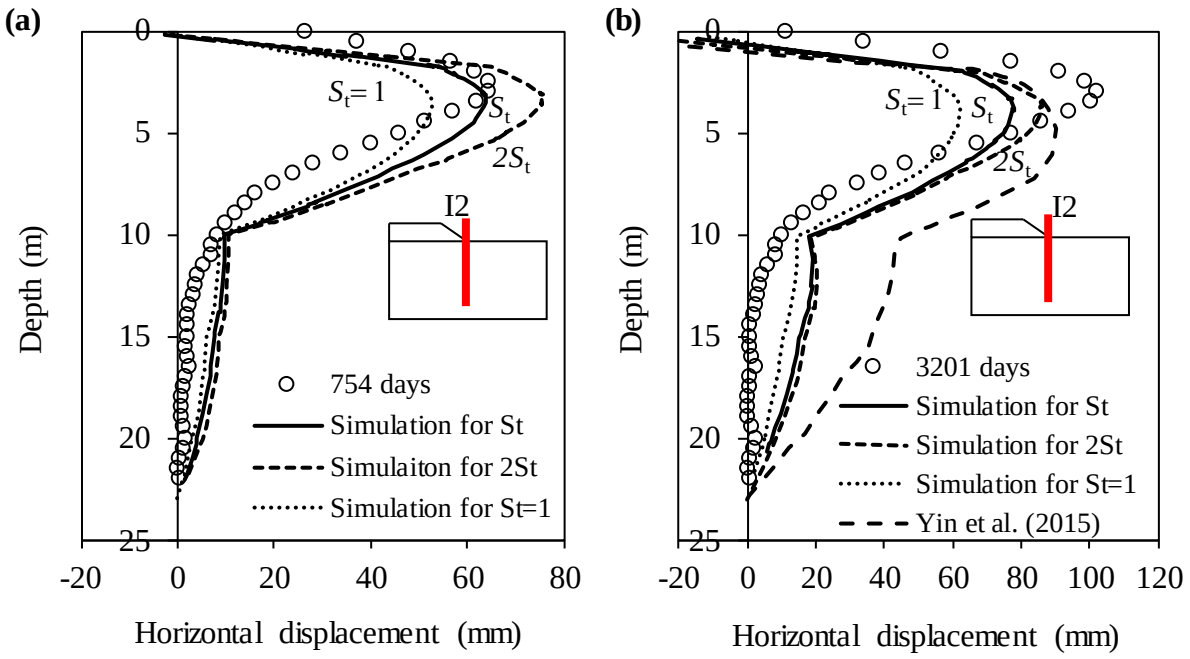
(a)
(b)
Depth (m)
Horizontal displacement (mm)
S_t= 1
S_t
2S_t
I2
754 days
Simulation for St
Simulaiton for 2St
Simulation for St=1
3201 days
Simulation for St
Simulation for 2St
Simulation for St=1
Yin et al. (2015)

Fig. 11

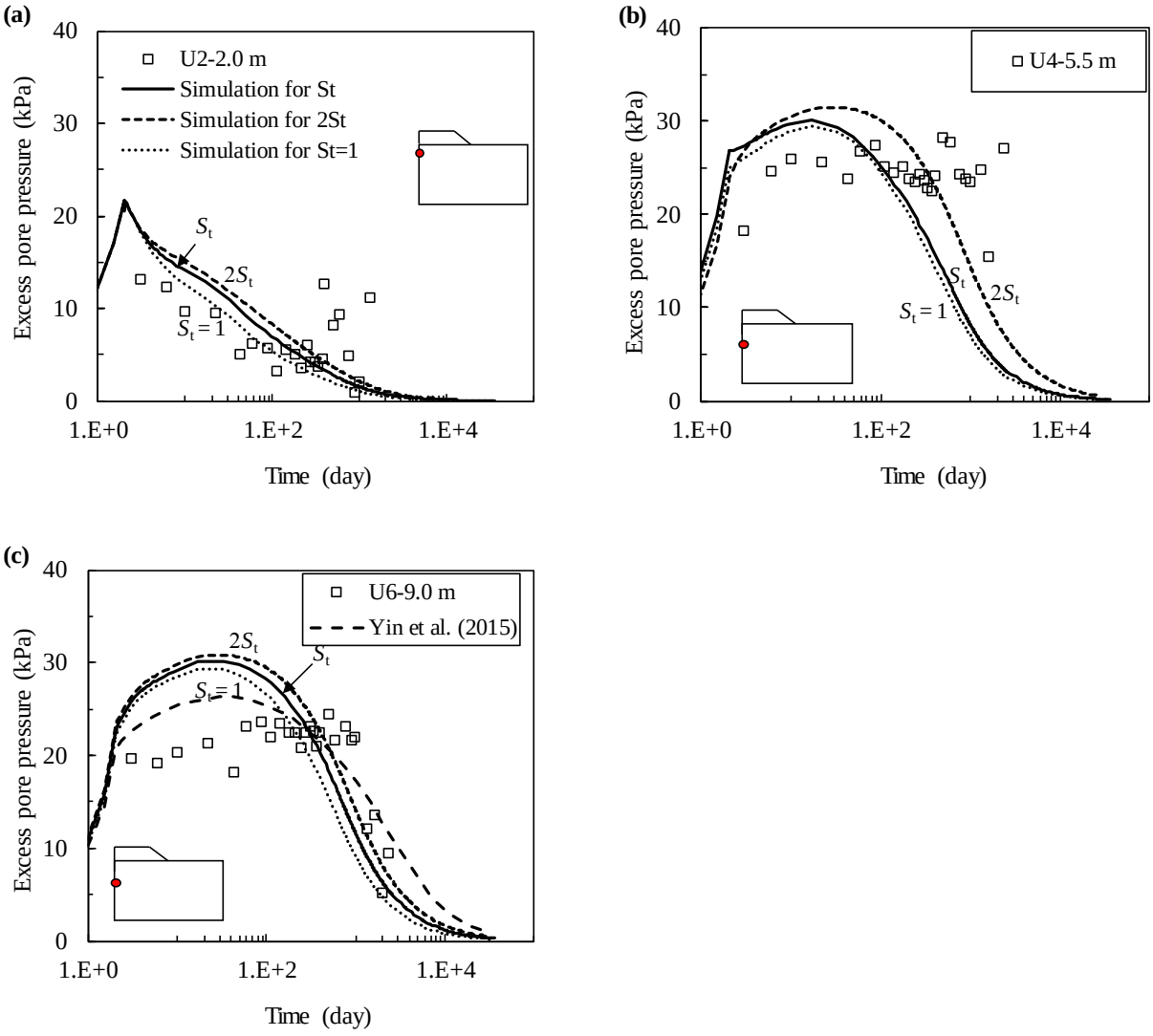
(a)
U2-2.0 m
Simulation for St
Simulation for 2St
Simulation for St=1
Excess pore pressure (kPa)
Time (day)
S_t
$2S_t$
$S_t = 1$
(b)
U4-5.5 m
(c)
U6-9.0 m
Yin et al. (2015)
1.E+0
1.E+2
1.E+4
0
10
20
30
40

Fig. 12

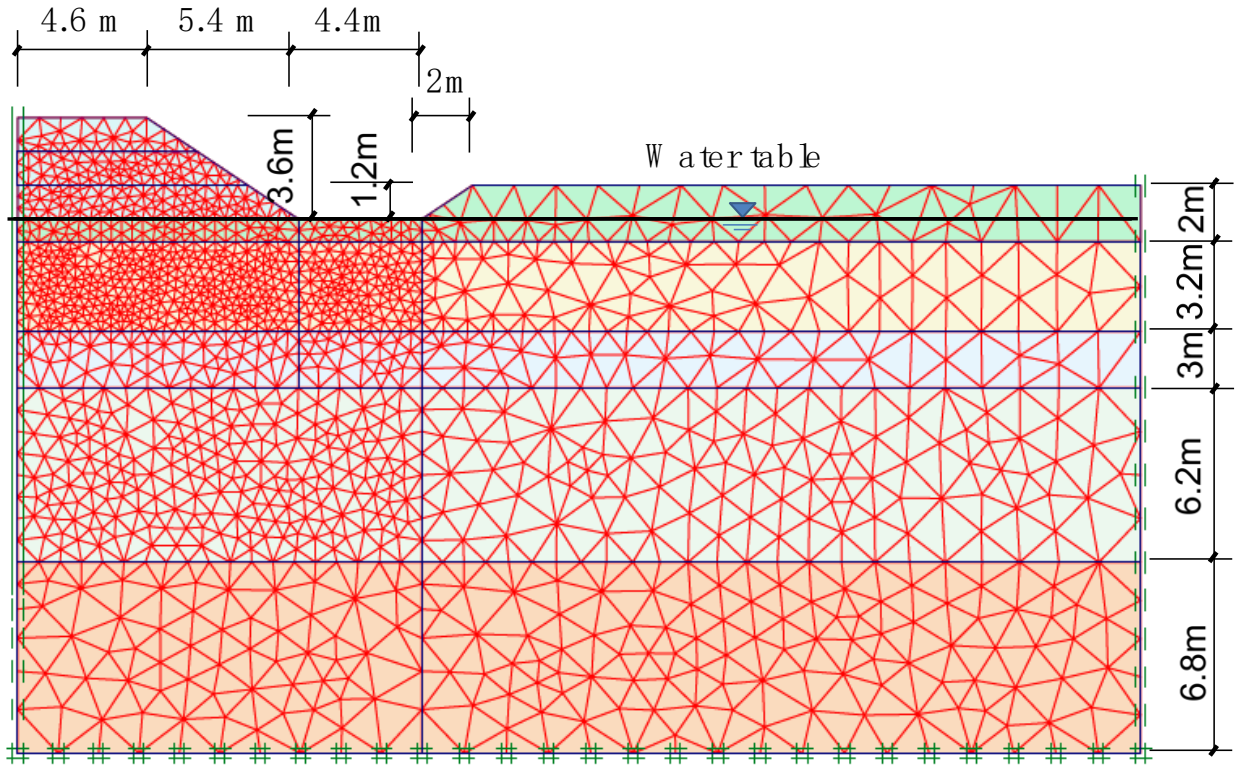

Fig. 13

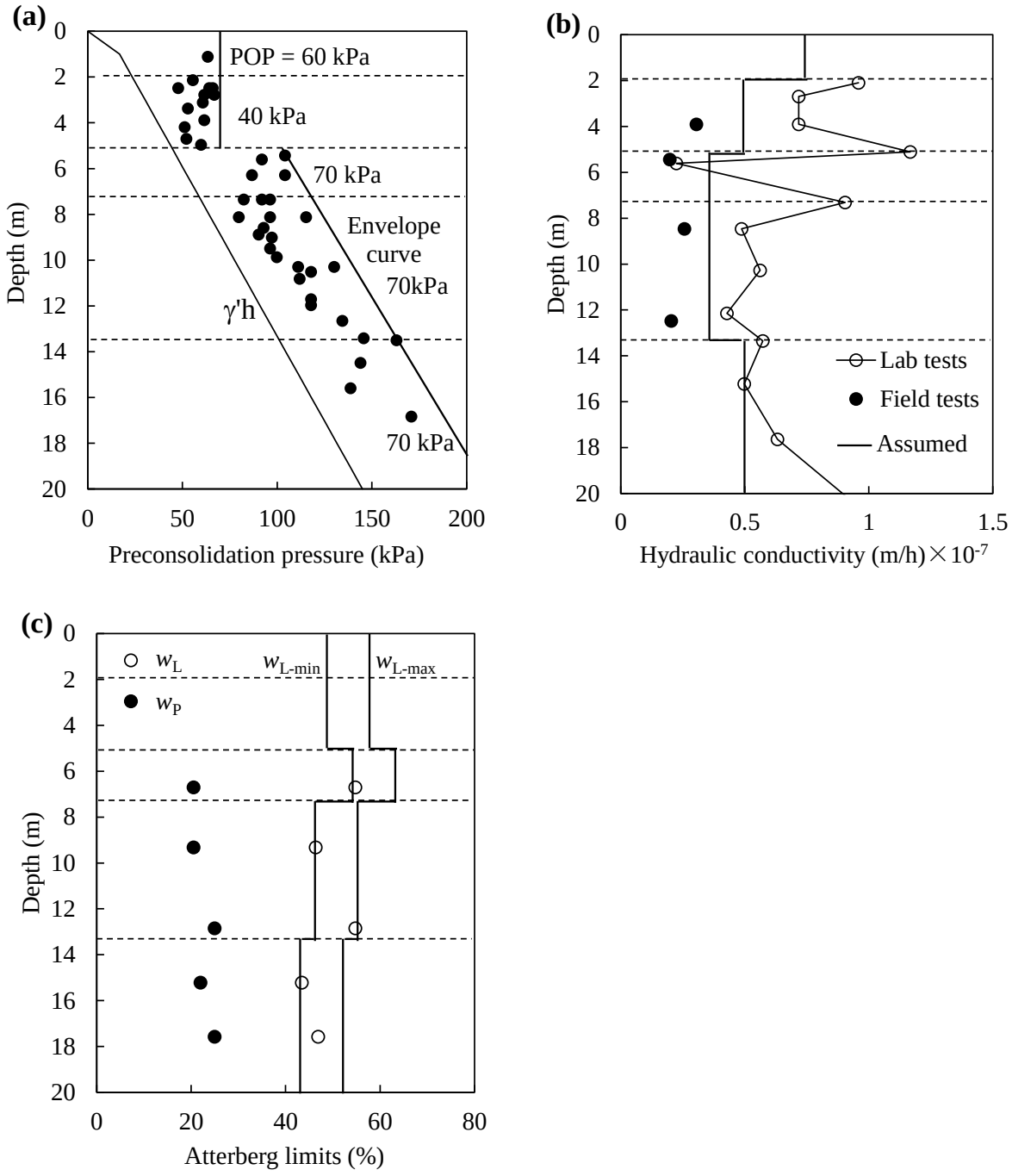
(a)
POP = 60 kPa
40 kPa
70 kPa
Envelope curve
70kPa
γ'h
70 kPa
Depth (m)
Preconsolidation pressure (kPa)
(b)
Lab tests
Field tests
Assumed
Depth (m)
Hydraulic conductivity (m/h)×10-7
(c)
wL
wL-min
wL-max
wP
Depth (m)
Atterberg limits (%)

Fig. 14

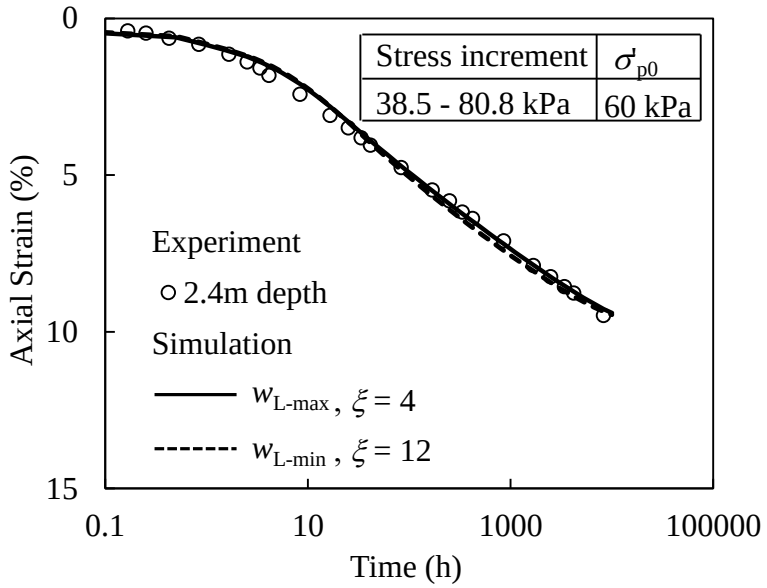
Stress increment
σ'_{p0}
38.5 - 80.8 kPa
60 kPa
Experiment
2.4m depth
Simulation
$w_{L\text{-}max}$, ξ = 4
$w_{L\text{-}min}$, ξ = 12
Axial Strain (%)
Time (h)
0
5
10
15
0.1
10
1000
100000

Fig. 15

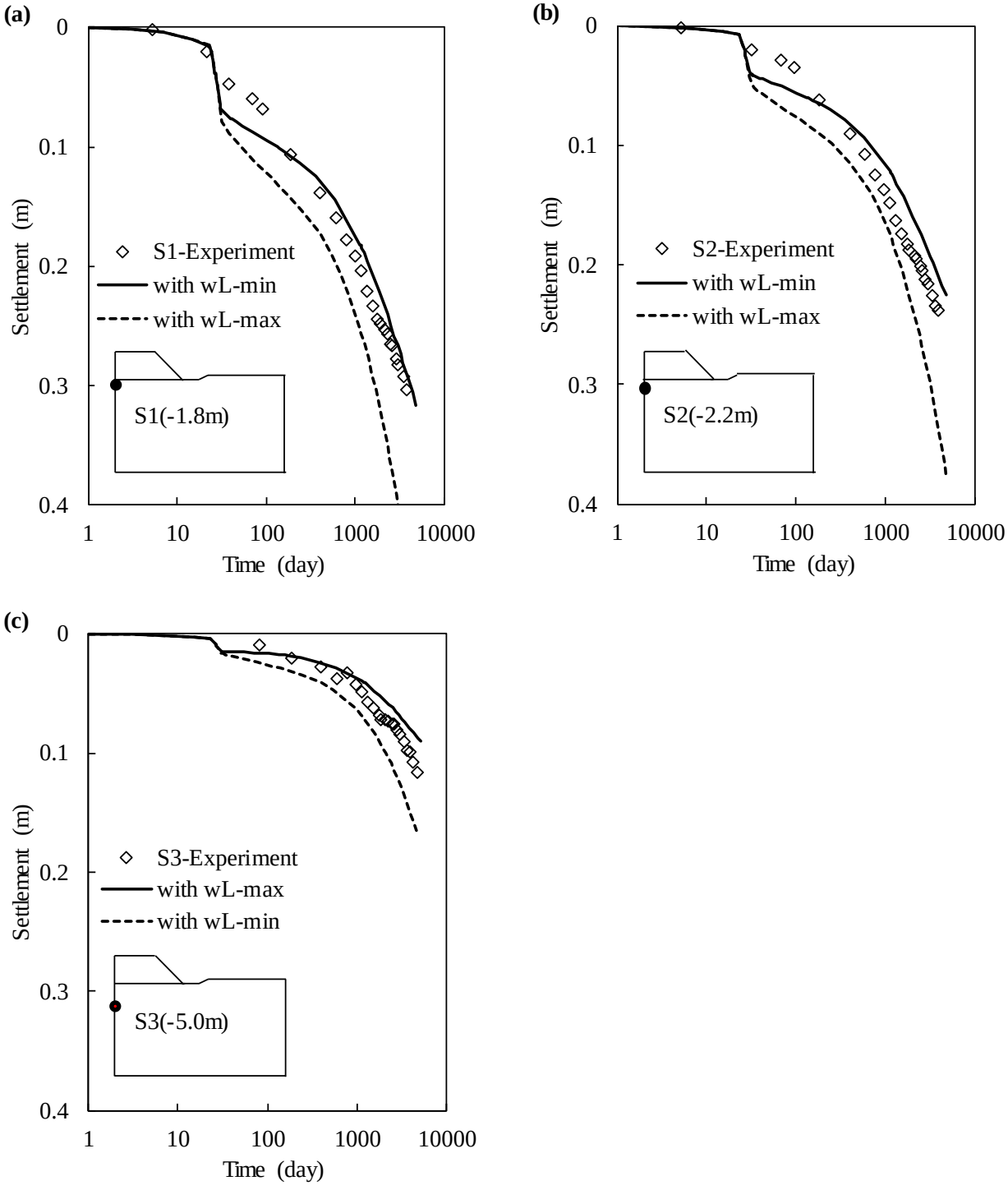
(a)
Settlement (m)
0
0.1
0.2
0.3
0.4
1
10
100
1000
10000
Time (day)
S1-Experiment
with wL-min
with wL-max
S1(-1.8m)
(b)
Settlement (m)
Time (day)
S2-Experiment
with wL-min
with wL-max
S2(-2.2m)
(c)
Settlement (m)
Time (day)
S3-Experiment
with wL-max
with wL-min
S3(-5.0m)

Fig. 16

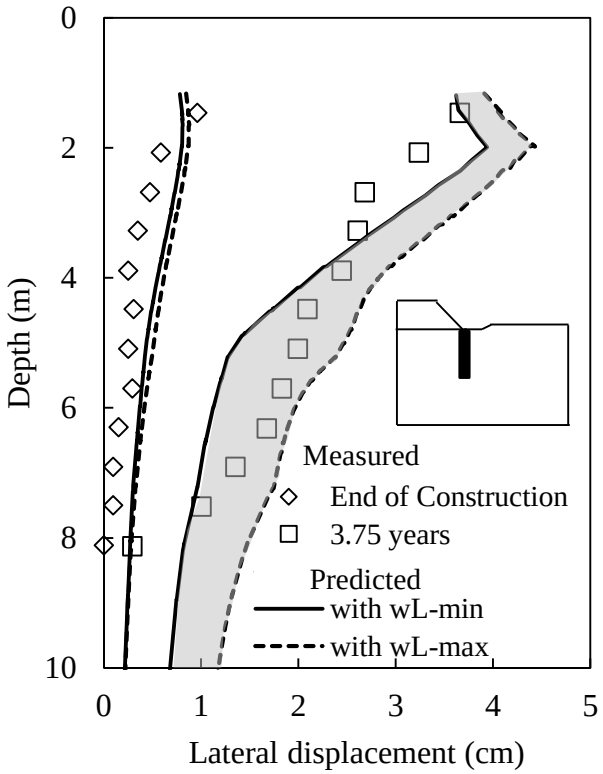
0
2
4
6
8
10
Depth (m)
0
1
2
3
4
5
Lateral displacement (cm)
Measured
End of Construction
3.75 years
Predicted
with wL-min
with wL-max

Fig. 17